Title

Development of an RNA aptamer as a therapeutic agent for synucleinopathies

Journal

Nature Communications

ISSN

2041-1723

Authors

Murakami, Kazuma
Van Nguyen, Thi Hong
Tsuda, Leo
et al.

Publication Date

2026-07-01

DOI

10.1038/s41467-026-75209-z

nature communications

Article

https://doi.org/10.1038/s41467-026-75209-z

Development of an RNA aptamer as a therapeutic agent for synucleinopathies

Received: 25 August 2025

Accepted: 23 June 2026

Published online: 15 July 2026

Check for updates

Kazuma Murakami[1] ✉, Thi Hong Van Nguyen[1], Leo Tsuda[2], Esha Chawla[3], Yangxia Wang[3], Yiran Chen[4], Nadia Stefanova[5], Chioko Nagao[6], Kenji Mizuguchi[6], Shouvik Manna[7], Samir K. Maji[7], Hidehito Tochio[4] & Gal Bitan[3,8,9]

The aggregation of α-synuclein (αSyn), a 140-mer protein, has been implicated in the pathogenesis of Parkinson's disease, multiple system atrophy, and dementia with Lewy bodies. KTKEGV pseudo-repeats (KRs) in the sequence of αSyn are key mediators of its prion-like propagation and neurodegeneration. Despite the availability of symptomatic treatments, no current therapy effectively delays disease progression. Here we report a 77-nucleotide RNA aptamer called 1R6, obtained through in vitro selection, that binds with high affinity and selectivity to αSyn1-95. 1R6 significantly inhibits αSyn oligomerization and β-sheet-rich fibril assembly and promotes disaggregation of preformed fibrils. Additionally, 1R6 suppresses αSyn seeding, as determined by a FRET-based biosensor-cell assay. Cellular studies reveal that 1R6 co-transfection completely prevents αSyn-induced cytotoxicity. To assess the protective effects of 1R6 in vivo, we use a Drosophila melanogaster model expressing human αSyn in neurons. Flies fed 1R6 show improved locomotor activity, reduced photoreceptor degeneration, and decreased αSyn levels in the head. Structural characterization using ^{1}H-^{15}N heteronuclear multiple quantum correlation nuclear magnetic resonance experiments demonstrates that 1R6 targets KR motifs, a finding further supported by in silico simulations. Our findings support further development of RNA aptamers, such as 1R6, including evaluation of efficacy, stability, delivery, and immune responses in mammalian systems, highlighting their potential as therapeutic candidates for synucleinopathies.

Misfolding and aggregation of amyloidogenic proteins are associated with several neurodegenerative disorders. The primary pathogenic protein in synucleinopathies, including Parkinson's disease (PD), dementia with Lewy bodies (DLB), and multiple system atrophy (MSA) is α-synuclein (αSyn)[1–3]. αSyn is the main component of Lewy bodies in patients with PD and DLB and glial cytoplasmic inclusions in MSA, and its toxic oligomers and aggregates are thought to be causative agents of neuropathology in these diseases[4]. Point mutations in, or

[1]Division of Food Science and Biotechnology, Graduate School of Agriculture, Kyoto University, Kyoto, Japan. [2]Kankyo Eisei Yakuhin Co. Ltd., Kyoto, Japan. [3]Department of Neurology, David Geffen School of Medicine, University of California Los Angeles, Los Angeles, CA, USA. [4]Department of Biophysics, Graduate School of Science, Kyoto University, Kyoto, Japan. [5]Division of Neurobiology, Department of Neurology, Medical University of Innsbruck, Innsbruck, Austria. [6]Institute for Protein Research, The University of Osaka, Ibaraki, Osaka, Japan. [7]Department of Biosciences and Bioengineering, Sunita Sanghi Centre of Aging and Neurodegenerative diseases (SCAN), Indian Institute of Technology Bombay, Powai, Mumbai, India. [8]Brain Research Institute, University of California Los Angeles, Los Angeles, CA, USA. [9]Molecular Biology Institute, University of California Los Angeles, Los Angeles, CA, USA. ✉e-mail: murakami.kazuma.4v@kyoto-u.ac.jp

multiplication of, the *SNCA* gene encoding αSyn cause familial PD[5–8]. αSyn oligomers cause neurotoxicity, synaptic impairment, mitochondrial dysfunction, endoplasmic reticulum stress, neuroinflammation, proteostasis dysregulation, and apoptosis, all of which lead to neuronal death[9]. αSyn aggregation involves formation of cross-β structures, typical of amyloid fibrils, and an enrichment in β-sheet formation has been reported already in rigid regions of high-order oligomers, before fibril formation[10,11]. The development of αSyn assembly modulators is believed to be a promising approach for inhibiting the abnormal self-assembly process, preventing the toxicity of αSyn oligomers and aggregates, potentially delaying the onset and slowing the progression of synucleinopathies.

αSyn is a 140-residue protein mainly located at presynaptic terminals[2,12]. Its amphipathic N-terminal region (residues 1–60) contains ~5.5 of seven imperfect repeats, each with a variant of a KTKEGV motif (a.k.a. KTKEGV repeat: KR), whereas the hydrophobic middle region (residues 61–95, known as the non-amyloid-β component (NAC) domain) is critical for the aggregation process and forms the core of the amyloid fibrils. The KR motifs contribute to the self-assembly and neurotoxicity of αSyn[13,14], as well as to its interactions with phospholipid membranes[15–17] (Fig. 1a). Eleven (73%) of the 15 Lys residues in αSyn are concentrated in the N-terminal region, whereas only one is in the NAC region and three Lys residues are in the C-terminal region (Supplementary Fig. 1). Cryo-electron microscopy has revealed the atomic structure of the N-terminal and NAC regions in αSyn filaments[18]. Structure-activity relationship[19] and nuclear magnetic resonance (NMR) studies[14] confirmed the critical role of these domains in αSyn aggregation. In contrast, the acidic, proline-rich C-terminal region (residues 96–140)[20] is not part of the amyloid core and is prone to cleavage during or after aggregation[21]. C-terminally truncated αSyn is abundant in Lewy bodies found in the brain of patients with PD or DLB[22,23].

Despite the functional significance of the αSyn N-terminal region, most commercially available anti-αSyn antibodies target the C-terminal region or its phosphorylated forms. Consequently, these antibodies may fail to detect or underestimate αSyn aggregates in

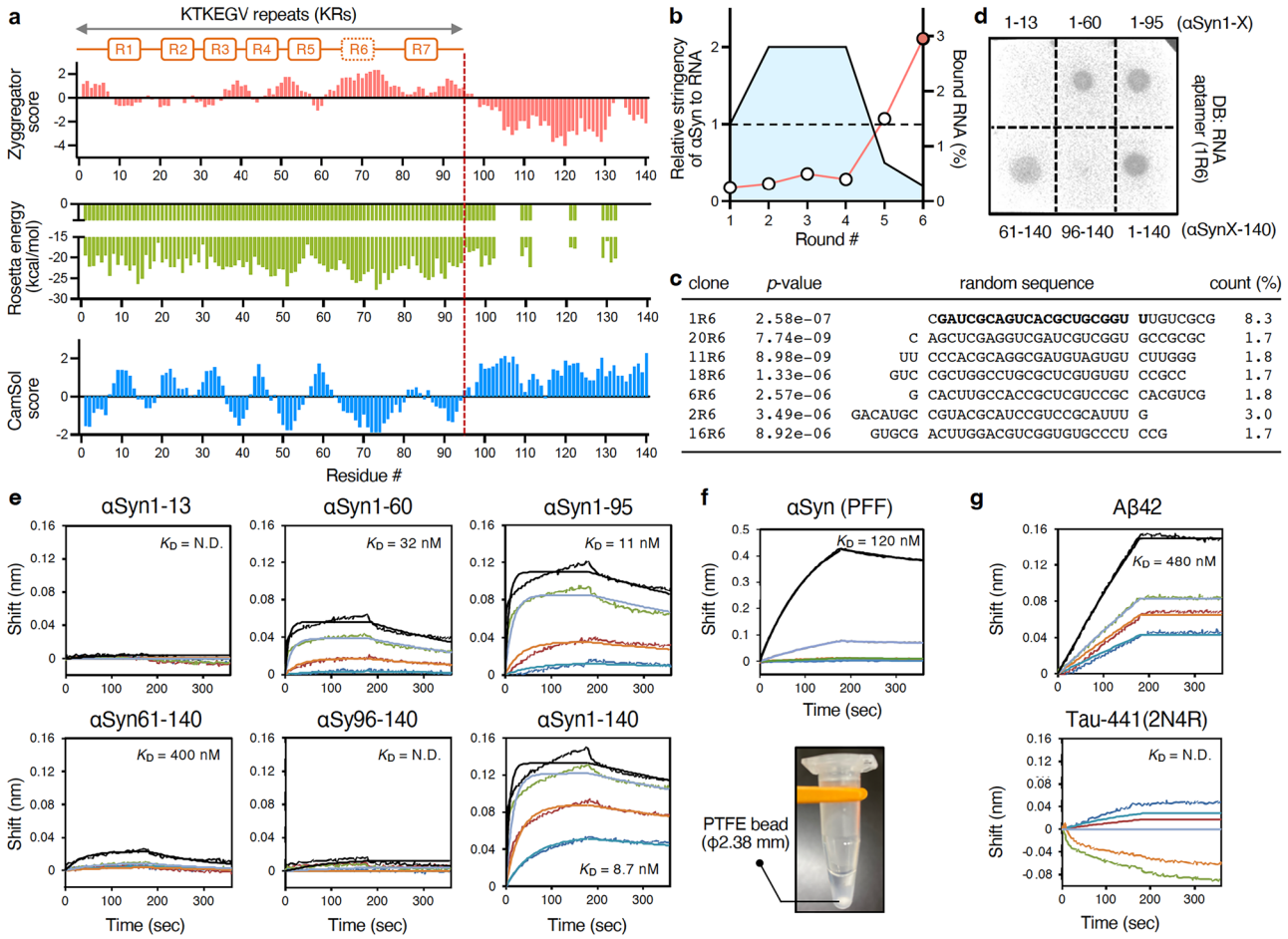

Fig. 1 | Selection of an RNA aptamer against αSyn1-95 and its binding characterization. a Aggregation and solubility profiles per amino acid in the αSyn sequence derived from Zyggregator score for aggregation propensity, Rosetta energy for protein structure, and CamSol score for water solubility. These profiles indicate that αSyn1-95 is aggregation-prone and point to a low-solubility region, which includes the seven imperfect KTKEGV repeats (KR). **b** UV measurement of SELEX progression. The ratio of bound RNA for each round of selection was plotted as a percentage of the total RNA used for the corresponding cycle (right y-axis). The ratio of αSyn to RNA between 1:2 and 1:0.25, respectively, is highlighted by the light blue area and left y-axis. **c** Alignment of the selected sequences within conserved family-1 (Supplementary Fig. 2) in the round-6 library of the αSyn1-95 SELEX cycle with the count (%) of the final library (18,540,679 reads). For the MEME analysis, the *p*-values represent the one-sided probabilities that an equal or better site would be found in a random sequence of the same length conforming to the background letter frequencies. The nucleotides in bold correspond to sh1R6. **d** Dot blots of αSyn fragments probed by 1R6. An aliquot containing 100 pmole of each αSyn fragment or full-length αSyn was blotted and probed with 0.3 μM of 1R6. BLI sensorgrams and curve fitting of 1R6 as a ligand to (**e**) αSyn fragments or full-length αSyn, (**f**) αSyn PFF, (**g**) Aβ42 or tau-441(2N4R) as the analyte at 200 nM (blue), 400 nM (orange), 800 nM (green), or 1600 nM (black). As shown in the lower panel of (**f**), PFFs were formed as a white precipitate by incubating 100 μM Syn1-140 in a buffer containing one PTFE bead (ϕ2.38 mm) in Protein LoBind® Tubes. N.D., not determined. Source data are provided as a Source Data file.

pathological analyses if their epitopes are in regions that are cleaved in the aggregates, highlighting the need to develop novel reagents that can specifically recognize the N-terminal region to improve diagnostic and therapeutic strategies for synucleinopathies. A recent study using an antibody against the N-terminus of αSyn (A15110D) reported the accumulation of αSyn aggregates in neuronal nuclei in MSA, which were difficult to detect using antibodies against pS129-αSyn[24].

Aptamers—single-stranded DNA/RNA oligonucleotides—offer similar binding affinity and specificity to antibodies, along with several advantages, such as small size, facile chemical synthesis (including large-scale production), high stability, and low immunogenicity[25]. These characteristics make aptamers attractive for molecular recognition, including of amyloidogenic proteins[26]. Moreover, RNA aptamers can be expressed in target cells, e.g., neurons, creating an in situ inhibitor that would inhibit aggregation and facilitate the degradation of amyloidogenic proteins, such as αSyn. However, generation of aptamers against amyloidogenic proteins is difficult because in the amyloid form, these proteins inherently bind with high affinity and low selectivity to nucleic acids[27–30]. Thus, to date, only three aptamers targeting αSyn have been reported: M5-15[31], recognizing αSyn monomers and oligomers; T-SO530[32], recognizing αSyn oligomers; and F5R1, recognizing αSyn fibrils[33], as reviewed by Murakami et al.[26] These aptamers target the aggregated states, yet the aptatopes (akin to antibody epitopes) they recognize have not been determined. Here, we detail the development of an RNA aptamer, 1R6. We also report that 1R6 mitigates αSyn aggregation and cytotoxicity in cellular models, explore the structural basis for αSyn recognition, and demonstrate that 1R6 improves motor function in a *Drosophila* model of synucleinopathy.

Results

Characterization of 1R6 as an RNA Aptamer against αSyn1-95

To identify key regions in αSyn contributing to its aggregation that could be attractive for aptamer development, we evaluated the sequence of the protein using three predictive tools: the Zyggregator score for aggregation propensity[34], Rosetta energy for structural stability[35], and CamSol score for solubility[36]. The results of these in silico analyses indicated that the KR motifs, clustered within αSyn1-95, are key contributors to the self-assembly of αSyn, in agreement with the previous reports[13,14] (Fig. 1a), leading us to choose αSyn1-95 as a target for aptamer selection. This region has been reported previously to aggregate into typical amyloid fibrils[37].

In each SELEX round, the refolded RNA pool was incubated with a nitrocellulose membrane spotted with 200–400 pmole αSyn1-95. Bound RNA was eluted by boiling in a detergent-containing buffer, reverse-transcribed, and amplified by PCR for the next round. During SELEX, selection stringency was increased by changing the molar ratio of αSyn1-95 to RNA, achieving significant enrichment after six rounds (Fig. 1b). The PCR products of the last round (round 6) were deep-sequenced, revealing one family (major family-1) and several ungrouped sequences (minor family-2 and family-3) among the top 20 sequences (Supplementary Fig. 2a). The MEME Suite analysis showed that the 77-nt sequence 1R6, which accounted for 8.3% of the final library, was selected from family-1 (Fig. 1c). The secondary structures of 1R6 were predicted using RNAstructure (Supplementary Fig. 2b). For 1R6, the conserved nucleotides were distributed in the internal stemloop (bold in Supplementary Fig. 2a and blue square in Supplementary Fig. 2b). Thus, we selected 1R6 for further testing and development.

To determine the specificity of 1R6 for different αSyn regions, dot blotting was performed using several αSyn fragments (Fig. 1d). FITC-labeled 1R6 bound to αSyn1-95, full-length αSyn, and αSyn1-60, but not to αSyn1-13 or αSyn96-140, and only weakly to αSyn61-140. A FITC-labeled monoclonal antibody specific for αSyn115-121 was used as a positive control and showed binding to αSynX-140, including αSyn61-140, αSyn95-140, and αSyn1-140, as expected (Supplementary Fig. 3).

To characterize the binding kinetics and binding affinity of 1R6 for αSyn, we used BLI. 5′-Biotinylated 1R6 was immobilized on a streptavidin biosensor, and αSyn was added to the solution. Stable complexes of 1R6 with αSyn1-95 formed, exhibiting a dissociation constant (K_D) = 11 nM. The affinity for full-length αSyn was slightly higher (K_D = 8.7 nM) (Fig. 1e, Supplementary Table 1). In agreement with the high affinity, the association kinetics (k_{on}) was fast, 8.6 $\times 10^4\,M^{-1}s^{-1}$, whereas the dissociation kinetics (k_{off}) was substantially slower, 1.5 $\times 10^{-3}\ s^{-1}$. Similarly, 1R6 demonstrated a high affinity for αSyn1-60 (K_D = 32 nM), which contains five KR motifs. In contrast, binding of 1R6 to αSyn1-13, αSyn61-140, or αSyn95-140, was markedly weaker, in agreement with the dot-blot results, suggesting that 1R6 binds primarily between residues 14-60 in α-syn but may also bind in the NAC region due to the similarity among the repeats in the NAC and N-terminal region. Notably, 1R6 bound avidly to mouse αSyn, which contains two amino acid substitutions in this region, as well as to the familial-PD, human αSyn variants A30P, E46K, G51D, A53E, A53T, and A53V, with K_D values of 4–12 nM (Supplementary Fig. 4, Supplementary Table 1), suggesting that these minor sequence variations had minimal impact on the binding of the aptamer. The affinity of 1R6 for αSyn PFFs was 14 times weaker than for monomeric αSyn (Fig. 1f) and its affinity for Aβ42 and tau-441(2N4R) was negligible (Fig. 1g), demonstrating the aptamer's selectivity for αSyn in its non-fibrillar form.

1R6 inhibits αSyn assembly in vitro

Given the high affinity of 1R6 for αSyn regions important for aggregation, we asked if the aptamer could inhibit aggregation. Aggregation of amyloidogenic proteins, including αSyn, typically follows nucleation-dependent polymerization dynamics, consisting of nucleation and elongation phases. Protein monomers gradually assemble into critical nuclei in the nucleation phase. Once nuclei are formed, the elongation phase proceeds, during which each nucleus serves as a template recruiting additional monomers, resulting in the formation of higher-order oligomers and ultimately amyloid fibrils[38,39]. Although thioflavin-T (Th-T) fluorescence typically is used to monitor the aggregation reaction, interference of RNA nucleotides with Th-T fluorescence[40], as reported in previous Aβ studies[41], prevents using this assay for studying the impact of aptamers. A simple solution is to replace Th-T with the related dye Th-S, which displays a sigmoidal increase in fluorescence reflecting the formation of the cross-β structure in amyloid fibrils. αSyn was used immediately after solubilization without pretreatment. Western blotting analysis detected only monomers (Supplementary Fig. 5a). 100 μM αSyn followed this behavior with a half-maximal fluorescence ($t_{1/2}$) = 42 h (Fig. 2a) and reached a plateau after ~70 h of incubation. Addition of 1R6 inhibited the aggregation reaction, as reflected by an extension of the lag phase (5 and 10 μM; $t_{1/2}$ = ~ 52 h) and reduction of the final fluorescence, reaching complete inhibition at 50 μM. Half-maximal inhibition (IC_{50}) was achieved at 15 ± 2.0 μM (Fig. 2a).

Morphologic analysis of αSyn in the absence or presence of 1R6 using TEM showed that αSyn alone formed typical long amyloid fibrils, and the addition of 1R6 resulted in dose-dependent inhibition of fibril formation (Fig. 2b), in agreement with the Th-S data.

To evaluate 1R6's ability to disaggregate PFF, 100 μM αSyn was allowed to aggregate for 14 days (Fig. 2c) before adding 50 μM 1R6 on Day 15, which led to a gradual decrease in Th-S fluorescence, demonstrating that 1R6 not only inhibited αSyn fibril formation, but also dissociated existing fibrils. Immuno-TEM confirmed the binding of the aptamer to the fibrils (Fig. 2c). R0 did not inhibit αSyn aggregation (Supplementary Fig. 6a) or disaggregate αSyn PFF (Supplementary Fig. 6b).

To further investigate the effect of 1R6 on αSyn assembly, we measured particle hydrodynamic radius using DLS and calculated the Z-average, an intensity-weighted mean diameter often used to characterize nanoparticle size in solution. On day 1, the main peak was at

https://doi.org/10.1038/s41467-026-75209-z

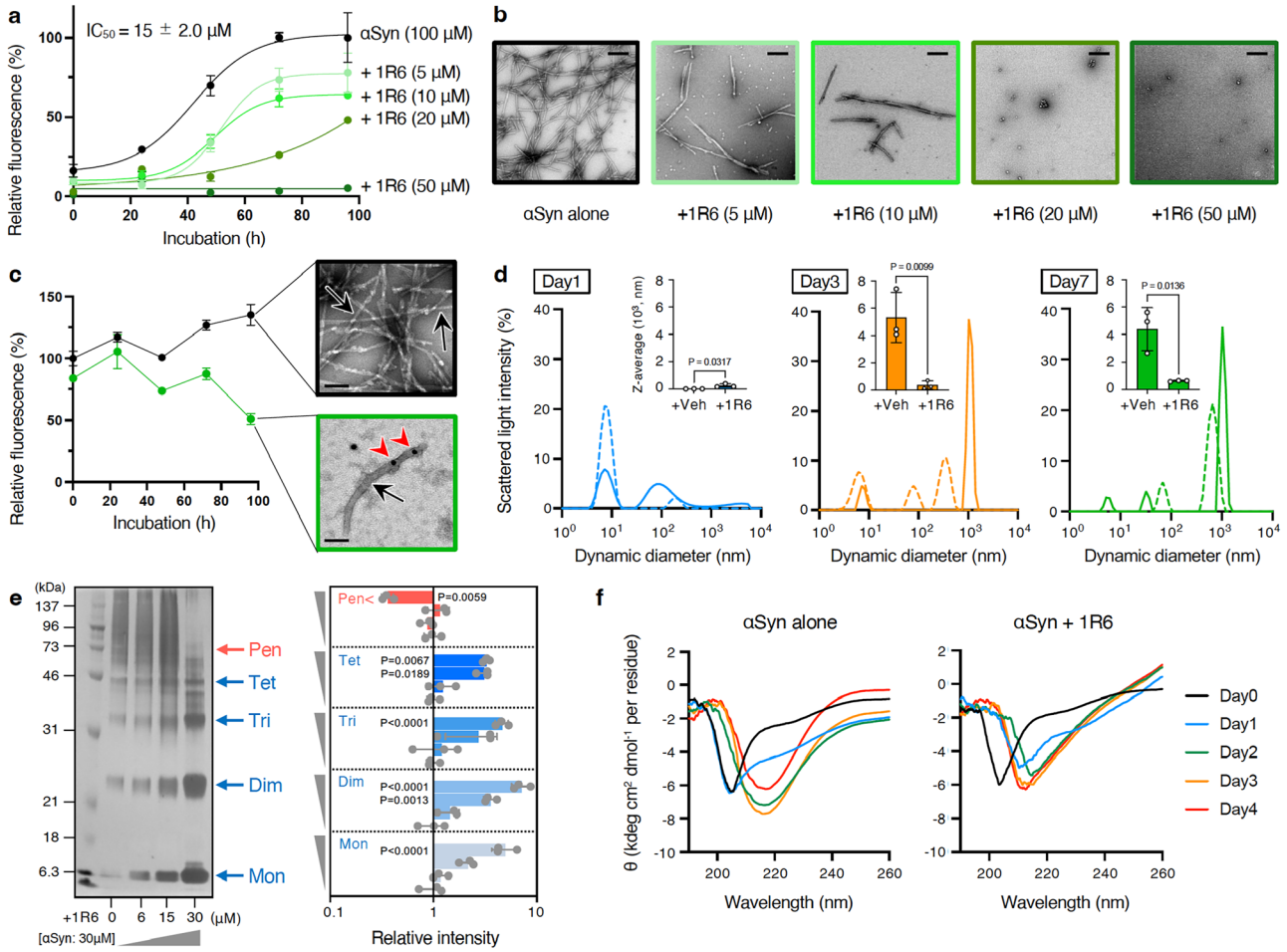

Fig. 2 | 1R6 inhibits αSyn oligomerization and aggregation in vitro. a Th-S assay of αSyn aggregation. 100 μM αSyn was incubated in the absence or presence of 5–50 μM 1R6 at 37 °C. The fluorescence values are normalized to that of αSyn alone at 96 h. **b** TEM analysis of αSyn at the end of the Th-S reactions shown in A. Scale bar = 200 nm. **c** Disaggregation of αSyn PFFs by 1R6. 100 μM PFFs were incubated at 37 °C in the absence or presence of 50 μM 1R6, and the reactions were monitored using Th-S fluorescence. After 96 hours, TEM images of gold-immunolabeled 1R6 were observed on the remaining fibrils. Scale bar = 100 nm. The red arrowheads and black arrows indicate gold nanoparticles and fibrils, respectively. **d** DLS analysis of αSyn oligomerization. 60 μM αSyn was incubated in the absence (solid line) or presence (dotted line) of 20 μM 1R6 at 37 °C. The inset shows the Z-average of the particles. Veh = vehicle. **e** PICUP analysis of αSyn oligomerization. PICUP was performed using 30 μM αSyn in the absence or presence of 6–30 μM 1R6. After crosslinking, the products were fractionated by SDS-PAGE and visualized by silver staining in the representative blot. The positions of the molecular weight markers are shown on the left. The percent abundance of N-mers ($N = 1–5$) was quantified densitometrically in triplicate samples and is shown in a logarithmic form. **f** Secondary structure analysis by CD spectroscopy. 100 μM αSyn were incubated in the absence or presence of 20 μM 1R6 at 37 °C. In panels (**a**, **c**–**e**), the data are expressed as mean ± SD (n = 3). P-values were calculated by a one-way ANOVA with post-hoc Dunnett test. Source data are provided as a Source Data file.

~10-nm diameter, whereas after incubation for 3 days, the main species observed had a 1–2 × 10^3-nm diameter, likely corresponding to amyloid fibrils[42], and which remained stable up to 7 days (Fig. 2d, solid line). In the presence of 1R6, the particle size distribution shifted toward smaller particles at all time points, suggesting inhibition of fibril formation and stabilization of smaller-diameter assemblies (Fig. 2d).

To further assess the oligomer order targeted by 1R6, we utilized PICUP[43–45]. Using this technique, crosslinked αSyn fractionated by SDS-PAGE and silver-stained appeared as a range of multiple species, which were resolved up to a pentamer and formed a high-molecular-weight smear at higher orders (Fig. 2e). Densitometric analysis revealed that 1R6 treatment attenuated the formation of pentamer and higher-order species in a dose-dependent manner and concomitantly increased the abundance of monomers, dimers, trimers, and tetramers (Fig. 2e).

The assembly of αSyn into high-order oligomers and amyloid fibrils is accompanied by the formation of β-sheet-rich structures[10,11]. To assess the effect of 1R6 on the temporal change in the secondary structure of αSyn, we used CD spectroscopy. The intensities of the maximum at ~200 nm and minimum at ~215 nm increased when αSyn was incubated alone, indicating a transformation from a statistical coil into a β-sheet-rich structure. In contrast, addition of 1R6 decreased those signals, indicating attenuation of this conformational transition, in agreement with the Th-S, TEM, DLS, and PICUP results.

1R6 Inhibits *In Cellulo* Seeding of αSyn

The prion-like, cell-to-cell transmission of αSyn through neuronal networks has been a major focus of recent research[46]. A previous study by Herrera-Vaquero et al.[47] demonstrated that αSyn aggregation could be seeded by brain extracts from an MSA mouse model, using a biosensor-cell assay based on FRET between CFP and YFP. In this assay, fusion proteins containing the PD-associated A53T-αSyn variant conjugated to CFP or YFP are expressed together in HEK293T cells[48]. In-cellulo assembly of αSyn in response to addition of pre-formed seeds (fragmented αSyn fibrils) can be visualized using fluorescence microscopy and quantified by flow cytometry. Bright puncta of αSyn aggregates were observed after incubating the biosensor cells with

https://doi.org/10.1038/s41467-026-75209-z

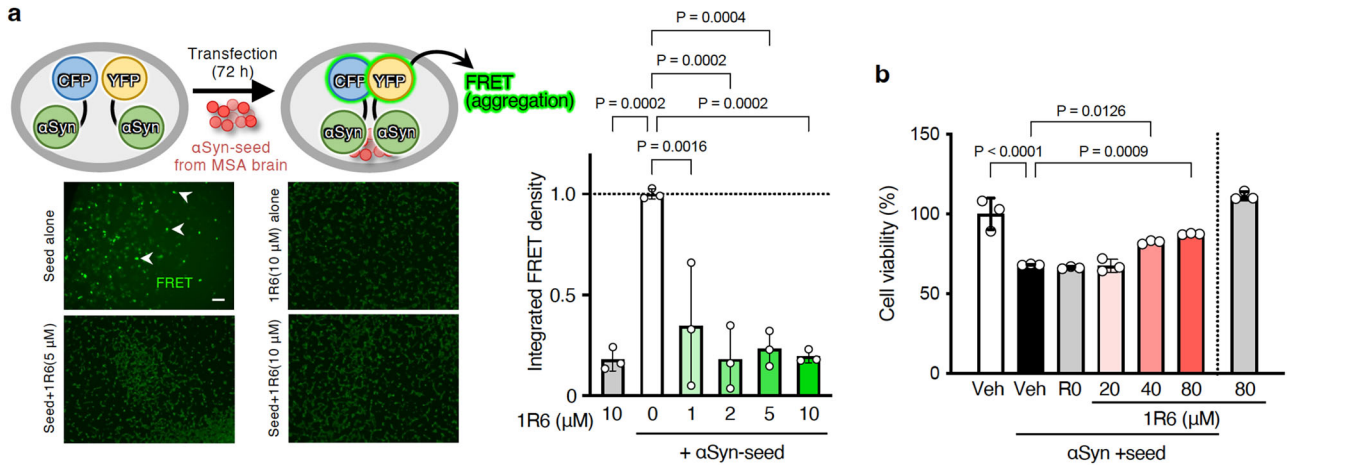

Fig. 3 | 1R6 inhibits αSyn seeding and cytotoxicity in cell culture. a αSyn seeding activity tested using FRET-based biosensor cells. Left (top), a schematic representation of HEK293T cells expressing CFP/YFP-conjugated αSyn. Cells were transfected with 20 μg αSyn PFFs in the absence or presence of 1–10 μM 1R6 mixed with Lipofectamine and incubated at 37 °C for 72 hours. Left (bottom), fluorescence-microscopy images of unseeded or seeded biosensor cells treated with 5 or 10 μM 1R6. Scale bar = 100 μm. Arrowheads indicate puncta. Right, integrated FRET density of biosensor cells. Data are expressed as the mean ± SD ($n = 3$ independent experiments). *P*-values were calculated by one-way ANOVA with post-hoc Dunnett test. **b** MTT assay of αSyn-induced cytotoxicity on HEK293T cells. 20 μM αSyn was transfected with 5 μg seed and 20 ~ 80 μM 1R6 mixed with Lipofectamine and incubated for 48 hours at 37 °C. Data are expressed as the mean ± SD ($n = 3$ independent experiments). *P*-values were calculated using one-way ANOVA with post-hoc Tukey test. *Veh* vehicle, *R0* initial RNA pool before selection. Source data are provided as a Source Data file.

MSA mouse brain extracts for 72 hours. Treatment of the seeds with 1R6 eliminated the formation of the bright puncta (Fig. 3a). FRET analysis demonstrated a marked reduction in the integrated fluorescence, which at 5 μM 1R6 was indistinguishable from baseline levels in the absence of the seeds (Fig. 3a). 1R6 treatment in the absence of seeds did not affect the fluorescence intensity. After incubating αSyn seeds with 1R6 inside liposomes for 24 h, we examined whether the aggregates remained intact using western blotting (Supplementary Fig. 5b). 1R6 dissociated the aggregates in the liposomes, indicating that 1R6 might prevent αSyn seeding derived from MSA mice within liposomes before they fully enter cells. These results show that 1R6 inhibits αSyn aggregation not only in vitro but also in a cellular environment.

1R6 inhibits αSyn-induced cytotoxicity

To determine whether 1R6 attenuated αSyn toxicity, we used the MTT assay in HEK 293 T cells. Although traditional cytotoxicity assays using exogenous αSyn are considered nonphysiological because of αSyn's predominant intracellular localization[49,50], as discussed above, extracellular αSyn oligomers and aggregates can trigger abnormal intracellular αSyn assembly, inducing toxicity. When αSyn was added exogenously to the culture medium in a liposome-encapsulated state at 20 μM and incubated for 72 hours, cell viability decreased by ~32% (Fig. 3b). This cytotoxicity was reduced significantly by 1R6 co-incubated with αSyn in a dose-dependent manner. 1R6 at the maximum concentration (80 μM) did not affect cell viability. The R0 RNA pool had no effect on the cytotoxicity of αSyn tested (Fig. 3b). Taken together, these results demonstrate that 1R6 inhibits not only αSyn self-assembly in vitro and in cultured cells, but also the cytotoxicity of the assemblies.

The concentration of αSyn seeds used in the biosensor cells was 7 ± 2 μM, whereas, in the MTT assay, to induce mitochondrial dysfunction allowing the measurement, 24 μM of αSyn was used. In addition to the 3.5-fold higher concentration used in the toxicity experiments, the downstream processes in these experiments are more complex than the simple aggregation that leads to the FRET signal in the biosensor cells. Inhibition of mitochondrial activity leads to reduced cell energetics, formation of reactive oxygen and nitrogen species, and damage to proteins, lipids, and nucleic acids. Although the relatively simple MTT assay does not measure all of these processes directly, because these downstream processes in turn further exacerbate the mitochondrial damage, it is reasonable that a higher concentration of the inhibitor would be needed to achieve a meaningful inhibitory effect compared to the simple inhibition of aggregation.

1R6 Reduces αSyn-induced neurodegeneration and motor dysfunction, and extends the lifespan in a Drosophila model of synucleinopathy

Given the preventive effects of 1R6 on αSyn aggregation and cytotoxicity, we examined its therapeutic potential in a *Drosophila* model expressing one copy of human wild-type αSyn and one copy of αSyn harboring an S129D pseudo-phosphorylation modification[51] in neurons. Neuronal S129D-αSyn expression at the adult stage was induced using the *GAL4/UAS/gal-80^{ts}* system with an *nSyb-Gal4* driver, which causes expression of the mutant gene upon increasing the incubator temperature from 18 °C to 29 °C (Fig. 4a)[52]. This enabled us to monitor the expression of native and pseudophosphorylated αSyn in adult neurons of living flies and measure the effects of expressing the human protein on fly behavior.

Impaired geotaxis is a behavioral measure reflecting neuronal dysfunction that can be assessed using a climbing assay[53]. *nSyb-Gal4/Y; UAS-αSyn^{S129D}/tub-gal80^{ts}; UAS-αSyn^{WT}/+* flies were treated with 1R6 mixed in their food starting 3 days after shifting the temperature to 29 °C to induce αSyn and S129D-αSyn expression, and their climbing ability was subsequently recorded on multiple time points until day 24 (Fig. 4b). Flies expressing αSyn showed significantly reduced climbing ability in an age-dependent manner after day 19, dropping to <60% of the level of *nSyb-Gal4/Y; tub-gal80^{ts}/+* control flies. Treatment with 50 μM 1R6 rescued significantly the decline in climbing ability on days 19 (from 53% to 76%), 21 (from 13% to 44%), and 23 (from 9% to 30%) (Fig. 4b, Supplementary Movie 1–10). The climbing ability of control flies, which do not express αSyn, remained nearly unaffected until day23 and declined significantly only on Day25 (Supplementary Fig. 7). αSyn expression in neurons shortened the flies' median (8%) and maximal (11%) lifespan significantly compared to control flies. In contrast, the lifespan of 1R6-treated flies was extended in a dose-dependent manner (Fig. 4c).

https://doi.org/10.1038/s41467-026-75209-z

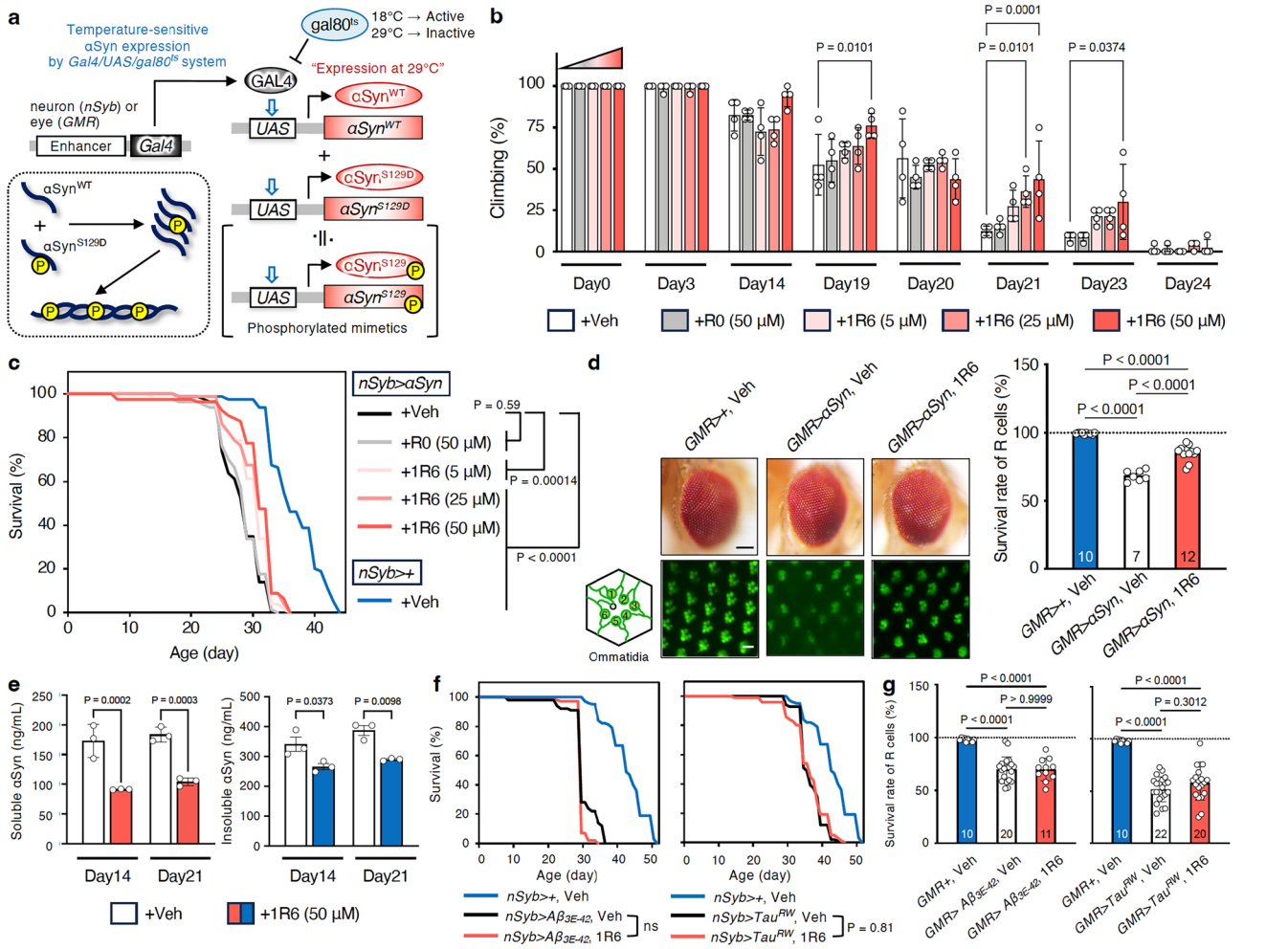

Fig. 4 | 1R6 rescues motor dysfunction and eye degeneration in a Drosophila model of synucleinopathy. a Overview of temperature-sensitive αSyn expression in *Drosophila* using the Gal4/UAS/gal80^{ts} system. Transgene expression was induced by the neuron-specific *nSyb* driver or eye-specific *GMR* driver. The introduced genes were wild-type αSyn and its mutant form encoding an S129D substitution as a phosphorylated mimetic of Ser129, facilitating the aggregation and toxicity of αSyn. **b** Climbing assay for motor function of the flies treated with 5–50 μM 1R6 or 50 μM R0. Data are expressed as the mean ± SD ($n = 4$). **c** Lifespan analysis of αSyn transgenic flies treated with 5–50 μM 1R6 or 50 μM R0, $n = 80$ per group. Kaplan–Meyer curve, log-rank test. **d** Degeneration test. Left (top), representative light microscopic images of the external eye morphologies of the flies. Scale bar = 100 μm. Left (bottom), representative fluorescence microscopic images of GFP-tagged rhodopsin1 in the ommatidia of the flies. Scale bar = 4 μm. Right, survival rate of R cells estimated from the number of GFP-positive cells in the compound eye of αSyn flies on Day14. Data are expressed as the mean ± SD. **e** ELISA analysis of αSyn using the TB-T-soluble and insoluble fractions of fly heads on Day14 or Day21. Data are expressed as the mean ± SD ($n = 3$). **f** Lifespan analysis of transgenic flies expressing human Aβ or tau and treated with 50 μM 1R6, $n = 100$ per group. Kaplan–Meyer curve, log-rank test. **g** Degeneration test. Survival rate of R cells estimated from the number of GFP-positive cells in the compound eye of flies expressing human Aβ or tau on day14. Data are expressed as the mean ± SD. Significance was determined by one-way ANOVA with post-hoc Sidak test (**b**) or with post-hoc Tukey test (**c**–**g**). *Veh* vehicle. *R0* initial RNA pool before selection. In (**d**) right and (**g**), the number of flies analyzed per group is indicated in the bar graphs. Source data are provided as a Source Data file.

To assess neurodegeneration, we expressed αSyn constitutively in the fly compound eye using the GMR-Gal4 driver, a system that has been used extensively to characterize fly models of neurodegenerative diseases[54]. Expression of αSyn caused disorganization of the ommatidia in the fly eyes, decreasing the number of GFP-positive photoreceptor cells (Fig. 4d). 1R6 treatment enhanced fluorescence levels significantly and restored ommatidia organization, demonstrating a protective effect of the aptamer on photoreceptor cells against αSyn-induced degeneration.

To investigate whether 1R6 affected soluble αSyn levels in the adult fly neurons, we extracted the soluble protein fraction from fly heads using a Triton X-100 lysis buffer and quantified αSyn by ELISA. Detergent-soluble αSyn concentrations in *UAS-αSyn/tub-gal80^{ts}* flies ranged between 150 and 200 ng/mL but were reduced significantly by 1R6 treatment (Fig. 4e). The soluble αSyn generated from 1R6-mediated disassembly of αSyn aggregates likely has been further degraded into small peptides or amino acids. The insoluble fraction also was reduced in the 1R6-treated group (Fig. 4e), implying an overall decrease in total αSyn levels in the fly heads. These observations suggest that the rescue of the synucleinopathy phenotype by 1R6 was associated with facilitating the clearance of the toxic protein.

In view of the selectivity of 1R6 for αSyn compared to Aβ and tau in vitro (Fig. 1g), we asked whether this selectivity was preserved in vivo. To address this question, we used flies expressing Aβ3-42^{E3Q}, an N-terminal pyro-glutamylated form of Aβ,[55] or tau^{R406W},[56] a mutant form of human tau that causes a familial form of frontotemporal dementia, using the same expression system. 1R6 did not recover the declined climbing ability of flies expressing Aβ3-42^{E3Q} (Supplementary Fig. 8a) or the lifespan of these flies (Fig. 4f). Using the GMR-Gal4 driver on GFP-tagged rhodopsin1 in R1-6 photoreceptor cells, Aβ expression caused ommatidia disorganization, which was not affected by 1R6 (Fig. 4g, Supplementary Fig. 8b). Similarly, 1R6 had no impact on the

https://doi.org/10.1038/s41467-026-75209-z

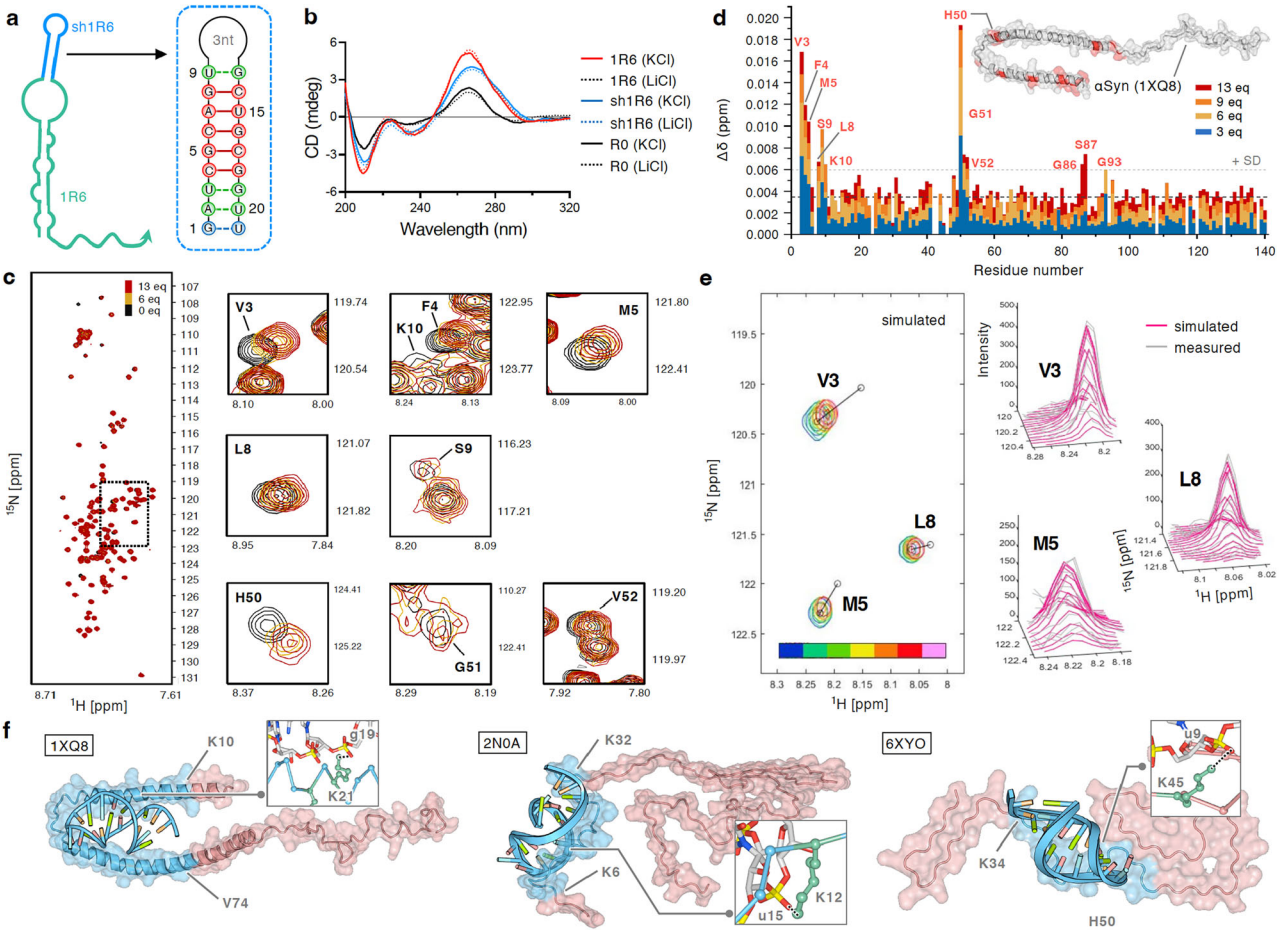

Fig. 5 | Structural insight into the recognition of αSyn by aptamer 1R6. a The position and sequence of sh1R6 in the full-length 1R6. **b** CD spectra of 5 μM 1R6, sh1R6, or R0 in the presence of 100 mM KCl (solid line) or LiCl (dotted line). NMR titration of αSyn with sh1R6. **c** HMQC spectra of 40 μM αSyn in the presence of 6 or 13 equivalents of sh1R6. The affected residues are highlighted in the dotted frame and expanded panels. **d** Chemical shift perturbation of αSyn upon the addition of 3, 6, 9, or 13 equivalents of sh1R6 was analyzed to determine the association of αSyn with sh1R6. Black and gray dotted lines indicate the mean and +SD, respectively. The residues whose chemical shift changes exceeded 1/2 of the SD values are indicated in red in the inset figure. **e** Left, simulated spectra of the affected residues V3, M5, and L8, in the expanded area in (**c**) (dotted square), also shown in Supplementary Fig. 9b. The 1R6 concentrations are color-coded, increasing from blue (low) to pink (high). The open circles indicate the predicted peak positions for each residue when all proteins are bound by RNA. Right, 3D comparison of the simulated and observed cross-peaks at V3, M5, and L8 in the presence of 13 equivalents of sh1R6. **f** Molecular docking of αSyn structures with the modeled sh1R6 generated from HADDOCK. The complexes with the lowest energy are shown in the contacted (blue) and uncontacted (red) regions. PDB codes of αSyn (1XQ8, 2N0A, and 6XYO) were used for docking calculations. The residue number indicates the number of residues from the start and end of the contact. Source data are provided as a Source Data file.

climbing ability, lifespan, or eye-toxicity phenotype in flies expressing tau^{R406W} (Supplementary Fig. 8c, Figs. 4f, 4g, and Supplementary Fig. 8d), demonstrating that 1R6 is a selective anti-αSyn agent.

Structural Insight into the αSyn–1R6 contact regions

Given the therapeutic effect of 1R6 on the pathological phenotypes of αSyn-expressing flies, we focused next on obtaining structural insight into the molecular interaction between the aptamer and αSyn. Two-dimensional NMR measurements were performed using ^{15}N-labeled αSyn solutions in the absence or presence of 1R6. Signal broadening in the 1H NMR spectra of 1R6 prevented unambiguous assignment of the RNA resonances, precluding structural analysis. Therefore, we took a reductionist approach next in an attempt to identify the most important part of the aptamer. RNAstructure, predicted that the conserved nucleotides within family-1 of the sequences enriched in the SELEX process, which are present in 1R6, a short, 21-base fragment of 1R6 that we named sh1R6, would form a stemloop structure (Fig. 5a, Supplementary Fig. 2). CD analysis showed that sh1R6, similar to the full-length 1R6, had minima at 210 and 235 nm and maxima at 220 and 270 nm (Fig. 5b), suggesting that the fragment maintained its structure outside the context of the full aptamer. The spectra did not change in the presence of KCl and LiCl, further supporting a stem-loop structure in sh1R6, as assessed using CD-NuSS. The structure contains eight intramolecular base pairs, as inferred from protons observed in 1D ^{1}H NMR[57] (Supplementary Fig. 9a). The CD (Fig. 5b) and NMR (Supplementary Fig. 9a) spectra of sh1R6 remained consistent throughout the measurements. In the CD spectra, the intensity of these peaks in the R0 pool of RNA, which was used as a control, was weaker than those in sh1R6 and 1R6 (Fig. 5b). Thus, we performed NMR experiments using the complex of αSyn with sh1R6 as an approximation of the binding between the protein and the full aptamer.

Assignment of the chemical shifts of ^{1}H-^{15}N HMQC spectra of ^{15}N-labeled αSyn was done based on previous reports deposited in BMRB, and was further confirmed by a series of standard triple-resonance NMR experiments (Fig. 5c). Titration of up to 13 equivalents of sh1R6 into the ^{15}N-labeled αSyn solution induced chemical shift perturbation of multiple residues, primarily in the amphipathic N-terminal region. Several residues, including V3, F4, M5, L8, S9, K10, H50, G51, and V52 showed substantial shifts of the corresponding ^{1}H-^{15}N peaks upon interaction with sh1R6. In addition, G86, S87, and

G93, all of which are small and relatively polar residues within the hydrophobic NAC region, showed dose-dependent shifts. These observations suggest the presence of three binding sites: 3–10, 50–52, and 86–93 (Fig. 5d, Supplementary Fig. 9b). In contrast, the perturbation in most of the C-terminal residue peaks was minimal. The simulated spectra, generated as contour plots and three-dimensional (3D) plots of V3, M5, and L8, supported the dose-dependent perturbation of the chemical shifts corresponding to these residues, enabling the estimation of K_D values in the micromolar range (Fig. 5e and Supplementary Figs. 10, 11). This K_D value did not fully align with the BLI results (Fig. 1e), likely due to differences in experimental setup, such as buffer composition, concentration range, or detection principles. These factors are further addressed in the Discussion section.

Chemical shift perturbations (CSPs) of αSyn titrated by sh1R6 identified three interaction sites: at the N-terminus - residues 3–10, in the pre-NAC region – residues 50–52, and in the NAC region – residues 86–93 (Fig. 5d). In addition, cross-peak intensities decreased throughout a sequence spanning from the N-terminus to residue 100 suggesting that the binding of sh1R6 is mediated primarily by contacts with the three 'hotspots' but affects the whole N-terminus and NAC regions (Supplementary Fig. 9c). Minimal broadening was detected in the C-terminal region, suggesting that this region is not involved in binding sh1R6.

Comparison of the NMR data to the BLI and dot blots suggests that at least two of the 'hot spots' are required for stable binding. Thus, despite the identification of the binding sites at residues 3–10 and 86–93, the short fragment αSyn1-13 did not bind 1R6 on its own and the longer fragment αSyn61-140 showed weak binding (Fig. 1d, e). In contrast, when both the N-terminal and pre-NAC regions were present, i.e., in αSyn1-60, stronger binding was observed, which was only slightly weaker than that of the fragment containing all three hot spots, αSyn1-95, or of full-length αSyn.

Using the structural constraints obtained from the NMR experiments, we conducted docking simulations using semiflexible, monomeric (PDB code: 1XQ8) or fibrillar (PDB code: 2N0A and 6XYO) αSyn with sh1R6 (Fig. 5f, see also Supplementary Fig. 12 for a list of all constraints) using the program HADDOCK[58]. It should be noted that the NMR structure of full-length αSyn (PDB 1XQ8) was obtained in the presence of 50 mM SDS, which is not a physiological condition. The simulations showed sh1R6 was embedded in a groove within residues 10–74 and 6–32, respectively. These grooves fit the binding sites, 3–10 and 50–52, revealed by NMR. The negative charges of the RNA phosphate groups may point away from the assembly surface and can be in close contact with Lys ε-amino groups upon fibril binding (Fig. 5f). sh1R6 exhibited an electrostatic anchor to the α-helical region, pointing toward the region K10-V74 in the monomeric structure, and toward two regions in the fibrillar structures, K6-K32 in PDB code 2N0A, and K34-H50 in PDB code 6XYO. For reference, the docking results conducted using 1R6 suggested the possibility of association with the groove within residues 10–74 and 6–32 in αSyn1-95 (Supplementary Fig. 13, see also Supplementary Fig. 14 for a list of all constraints). The docking results suggest that these combinations are structurally compatible with KR recognition during 1R6–αSyn interaction.

The electrostatic landscape inferred from the surface charge distribution of the KR region is partly consistent with the association of sh1R6 with the Lys-rich groove observed in the HADDOCK models, whereas in the docking analyses with Aβ42 or tau, no clear interactions with Lys or other residues were apparent (Supplementary Figs. 15 and 16). However, in contrast to the NMR-guided docking of αSyn, the docking analyses for Aβ42 or tau lacked experimental restraints and should be regarded as exploratory. The computational models alone may not fully account for the electrostatic basis underlying the specificity observed in the binding or fly experiments, but the models do support the association of the Lys-rich groove with 1R6.

Discussion

In this study, we identified and characterized an RNA aptamer, 1R6, that selectively targets the N-terminal and central regions of αSyn (αSyn1-95), particularly the lysine-rich domain containing the seven KR motifs, which plays a critical role in αSyn's aggregation and toxicity[59]. Truncation of the C-terminal region by 11 to 37 residues increases the aggregation rate of αSyn[60,61], supporting the role of αSyn1-95 in the aggregation. Recent bioinformatics and NMR studies have identified the P1 (residues 36–42) and P2 (residues 45–57) motifs as master controllers of αSyn assembly[14], both of which are contained within αSyn1-95. Given that αSyn1-95 itself forms typical amyloid fibrils[37], it is important to develop compounds recognizing this region and potentially inhibiting its self-assembly. Despite efforts in this direction, including an antibody targeting the N-terminus (αSyn1-10)[62], such compounds are relatively scarce, as most available antibodies have been developed against the C-terminal region.

Immune-based therapeutics are advancing into clinical trials[63]. The monoclonal antibody cinpanemab, which targets the N-terminal region of αSyn, has been explored clinically; unfortunately, it did not demonstrate clinical or imaging efficacy in patients with early PD compared with placebo[64]. Other modalities currently in preclinical development include α-helical peptides[65], cyclic peptides[66], and macrocyclic peptides[67]. However, the binding sites for these peptides have not been identified, and it is not known whether they bind to the N-terminus or NAC regions as does aptamer 1R6.

Our results demonstrate that 1R6 exhibits nanomolar-range binding affinity for αSyn1-95 and full-length αSyn, inhibits formation of high-molecular-weight oligomers and β-sheet-rich fibrils, and disaggregates pre-formed fibrils in vitro. In cellulo, 1R6 suppresses αSyn seeding activity and cytotoxicity in HEK293T cells. Importantly, in a Drosophila model of synucleinopathy, 1R6 mixed in the food ameliorates motor dysfunction, extends lifespan, and prevents photoreceptor degeneration. These protective effects correlate with a reduction in detergent-soluble αSyn levels in fly heads, suggesting that aptamer binding modulates αSyn proteostasis, inhibiting formation of toxic assemblies and facilitating their clearance.

CD and ^{1}H-NMR analyses suggest that 1R6 folds into a conserved RNA stem-loop structure in the region corresponding to sh1R6. The interaction between sh1R6 and αSyn was observed in ^{1}H-^{15}N HMQC NMR titration experiments, where dose-dependent chemical shift perturbations were observed in three regions: 3–10, 50–52, and 86–93. The model of the bound complex, generated using HADDOCK docking, suggests that the binding is driven by electrostatic interactions between the negatively charged phosphate groups in the RNA backbone and the positively charged lysine residues in KR motifs. These interactions likely contribute to 1R6's ability to inhibit the assembly of αSyn into oligomers and fibrils. Future high-resolution analyses, e.g., using cryo-EM, will help identify the minimal interactions required for the high affinity and selectivity of the aptamer, allowing optimization for improvement of the inhibition efficiency and long-term stability of 1R6. Consistent with the NMR data, the aptamer binds to the pre-NAC cluster in the monomer structure; however, docking results remain hypothesis-generating and require further 3D structural validation.

The NMR data suggest that the interaction of 1R6 with αSyn may be driven by electrostatic forces between the aptamer phosphate groups and the ammonium groups of Lys residues. Whereas the binding affinity measured via BLI yielded a K_D of 8.7–32 nM, the value estimated from the NMR titration was in the micromolar range. This discrepancy is not unexpected and can be attributed to the inherent differences between the two methods, particularly the vast difference in αSyn concentration, which in turn determines the aptamer concentration needed for binding measurement. BLI measures real-time binding kinetics in a surface-immobilized format, whereas NMR monitors solution-based chemical environment changes in a dynamic equilibrium. Differences in buffer composition also may contribute to the

differences in the measured binding affinity. BLI measurements involve ligand immobilization on a sensor surface, which can in part restrict conformational freedom and effectively increase the local ligand concentration, often resulting in stronger apparent affinities. In contrast, NMR titration experiments are performed entirely in solution and report on CSPs and changes in peak intensities, which typically reflect averaged populations and may emphasize weaker-binding conformers. Taken together, the apparent discrepancy between the NMR titration and BLI results may reflect the different features of the assays used, probing dynamically interacting states or highly stable states[68–70].

The affinity of 1R6 is in the same range as the DNA aptamers F5R1 and F5R2[33], which target the full-length αSyn. Hmila et al. developed another DNA aptamer (Apt11) specific for C-terminally truncated αSyn fibrils, but not monomers.[71] Apt11 binds αSyn fibrils generated from the truncated forms 1–107, 1–115, 1–122, and 1–130, as well as full-length αSyn fibrils. It inhibits αSyn-seeded aggregation in vitro, retards αSyn-seeded aggregation seeded by brain homogenates from patients with PD in a real-time quaking-induced conversion assay[72], and reduces formation of insoluble, αSyn phosphorylated at Ser129 (pS129-αSyn) in HEK293 cells[71].

Zheng et al. used F5R1 to demonstrate that the use of an internalization carrier molecule is effective for transporting aptamers to the brain[33]. F5R1 attached to a peptide carrier[73] enhanced membrane accessibility, inhibited cellular aggregation, and inhibited the cytotoxicity of αSyn overexpressed in primary neurons[33]. A follow-up study showed that F5R1 encapsulated in exosomes isolated from HEK293T cells could be delivered into mouse brain, where it suppressed αSyn aggregation in the substantia nigra and rescued motor dysfunction[74]. These exciting results demonstrate the therapeutic utility of anti-αSyn aptamers and support further development of 1R6. Moreover, because 1R6 is an RNA aptamer, a potential future therapeutic use is its expression in the brain following delivery, e.g., using adenoviruses, similar to current gene-therapy approaches.

To demonstrate the specificity of 1R6 in vivo, we generated *Drosophila* models that express three prominent amyloidogenic proteins, αSyn, Aβ, and tau. These models can be useful in future studies by other groups who wish to test the selectivity of their own candidate compounds targeting any of these proteins. In our study, 1R6 selectively mitigated climbing defects and photoreceptor degeneration in the synucleinopathy model, but not in the models expressing toxic forms of Aβ or tau, highlighting its specificity and therapeutic potential. Given the growing focus on mixed pathologies arising from the co-aggregates of amyloids in neurodegenerative diseases[39,75–77], the models developed here may also be used for testing compounds with broader activity against multiple amyloidogenic proteins. As with other biologics, challenges remain in DNA/RNA aptamer drug development, particularly with respect to stability, delivery, and immune stimulation[25,26]. The fly experiments do not allow us to unambiguously discern whether 1R6 primarily affects aggregation nucleation, propagation, or both, although we observed a reduction in total αSyn levels, including both soluble and insoluble fractions, which suggests enhanced clearance as a plausible explanation. The Th-S assay showed that 1R6 both prolonged the lag phase and reduced the rate of exponential fibril growth, indicating that in vitro, the aptamer interferes with both aggregation nucleation and elongation processes. Presumably, similar mechanisms operate in vivo, yet direct evidence is difficult to obtain at this stage.

In conclusion, our study presents an RNA aptamer disrupting αSyn aggregation and associated cytotoxicity. These inhibitory effects support the selection of αSyn1-95 as the SELEX target, as predicted by in silico analysis. Notably, 1R6 preferentially binds to αSyn and decreases αSyn concentrations selectively compared to other amyloidogenic proteins, such as Aβ and tau, both in vitro and in vivo. The present results provide a basis for the development of nucleic acid–based therapeutics against αSyn-related disorders such as PD. Future studies should explore further the mechanism of action of 1R6 in vivo, as well as the pharmacokinetics, stability, and delivery mechanisms of 1R6 and its derivatives in mammalian models.

Methods

Selection of RNA aptamer

RNA aptamers were selected using systematic evolution of ligands by exponential enrichment (SELEX)[41]. A DNA library was designed containing a 29-nt randomized region (A:T:G:C = 25%:25%:25%:25%) flanked by non-random 5′- and 3′-primer regions, and 3-nt thymine linkers between the randomized and primer regions: 5′-TAG AGA TAA TAC GAC TCA CTA TAG GGA CGA AGA CCA ACT GAA C -ttt-N_{29}-ttt-GTC CGT GCT GCC ACC TTA CTT C-3′. The DNA library and primers were purchased from Eurofins (Tokyo, Japan). Polymerase chain reaction (PCR) was performed to amplify the library in 20 cycles, each comprising 10 s at 98 °C for denaturing, 30 s at 53 °C for annealing, and 5 s at 72 °C for extension using the TaKaRa Ex Taq Hot Start Version kit on a TaKaRa PCR thermal cycler Dice Mini (TaKaRa Bio; Shiga, Japan). Double-stranded DNA was purified using the NucleoSpin Gel and PCR Clean-up kit (TaKaRa Bio). The initial RNA pool (R0) was generated via in-vitro transcription using the CUGA7 Kit (Nippon Gene, Tokyo, Japan) and purified using FastGene RNA Premium Kit and FastGene™ miRNA Enhancer (Nippon Genetics, Tokyo, Japan). RNA integrity was confirmed by electrophoresis on 6% Tris–borate–ethylenediaminetetraacetic acid (EDTA)–urea acrylamide gels (Invitrogen; Carlsbad, CA, USA) stained with SYBR Green II (TaKaRa Bio). In the SELEX or binding assays, RNA was quantified using a UV BioPhotometer (Eppendorf; Hamburg, Germany) or EzDrop 1000 C (Blue-Ray Biotech, Taiwan). As an experimental control, we used the original RNA library before the SELEX enrichment (R0). In this library, the RNA pool was created by in vitro transcription of scrambled ssDNA and the contribution of the active aptamer(s) is infinitesimally small. This is a widely accepted practice proposed by McKeague et al.[78]

Recombinant αSyn fragments, including αSyn1-60, αSyn1-95, αSyn61-140, and αSyn96-140, full-length human αSyn, and full-length mouse αSyn, tau-441(2N4R), and Aβ42 were purchased from rPeptide (Watkinsville, GA, USA). αSyn variants, including A30P, E46K, G51D, A53E, A53T, and A53V, were prepared as described previously[79]. αSyn1-13 was purchased from Cambridge Research Biochemicals (Cleveland, UK). The RNA pool or aptamers were denatured at 90 °C for 10 min and rapidly renatured on ice for 30 min for refolding before use.

αSyn1-95 (200–400 pmoles) was applied to a nitrocellulose membrane (0.2-μm pore size, Bio-Rad; Hercules, CA, USA). The renatured RNA pool was incubated with the αSyn1-95-spotted membrane in 200 μL Tris buffer (TB: 10 mM Tris-HCl, 100 mM KCl, pH 7.5) on a rotator at 25 °C for 1 hour. After washing with TB, the bound RNA was denatured in TB containing a detergent (TB-T: 10 mM Tris-HCl, 1 mM EDTA, pH 7.5, 0.05% Tween-20) at 90 °C for 10 min and collected by ethanol precipitation. Purified RNA was reverse-transcribed and amplified by PCR. The αSyn1-95:RNA molar ratio gradually changed from 1:1 (round 1) to 2:1 (rounds 2–4), 1:2 (round 5), and 1:5 (round 6).

Sequencing of RNA aptamers and prediction of secondary structure

Following bound RNA enrichment and RT-PCR, the Amplicon DNA library was prepared using the TruSeq Nano DNA Kit (Illumina, San Diego, CA, USA) and analyzed via next-generation sequencing using NovaSeq6000 (Illumina; San Diego, CA, USA) at Macrogen Japan Corp. (Tokyo, Japan). The obtained sequences were processed using AptaSUITE (https://drivenbyentropy.github.io/) and MEME Suite (https://meme-suite.org/meme/) for alignment, clustering, classification, and local super-motif analysis. RNA secondary-structure motif prediction was performed using the energy minimization algorithm of RNAStructure (https://rna.urmc.rochester.edu/RNAstructure.html).

Dot Blotting

Full-length αSyn or αSyn fragments, each at 100 pmole, were applied to a 0.2-µm pore size nitrocellulose membrane (Bio-Rad), and the membrane was blocked using Blocking Reagent for Can Get Signal (TOYOBO, Tokyo, Japan). After washing, the membrane was probed with0.3-µM fluorescein isothiocyanate (FITC)-labeled aptamer or 0.5 µg/mL anti-αSyn115-121 antibody (clone LB509, lot No. B360970, BioLegend, San Diego, Japan) at 25 °C for 1 hour. Chemiluminescent imaging was performed using LuminoGraph II (ATTO, Tokyo, Japan). For aptamer-based detection, the VariRays II apparatus (ATTO) was employed as the epi-illumination light source. TB-T was used as a washing buffer.

Bio-Layer Interferometry (BLI) measurements

BLI experiments were conducted at 30 °C with shaking at 1000 rpm using an OctetRED96 (ForteBio; Menlo Park, CA, USA)[41]. RNA aptamers were biotinylated using the 5′ EndTag Nucleic Acid Labeling System (Vector) with biotin-PEG6-maleimide (TCI) according to the manufacturer's protocol. Biotinylated RNA aptamers were immobilized on a streptavidin biosensor, and the biosensor was rehydrated at 30 °C with shaking at 1000 rpm in phosphate-buffered saline (PBS: 8.1 mM Na_2HPO_4, 1.5 mM KH_2PO_4, 2.7 mM KCl, 14 mM NaCl, pH 7.4) for 10 min. The immobilization was accomplished using 200 µL of 1 µM biotinylated aptamers in a 96-well black plate for 840 s, followed by incubation of the sensor in PBS buffer for 180 s. The binding reaction was performed in 200 µL TB containing αSyn concentrations ranging between 200 and 1600 nM for 180 s. Samples without protein were subtracted as background. The sensorgrams were generally fitted to a 1:1 binding model contingent on the lower chi-square coefficient, with association rate k_{on}, dissociation rate k_{off}, and dissociation constant K_D, determined using Data Analysis Software (ForteBio). A chi-square coefficient, which represents the sum of the squared deviations between the experimental data and the fitted curve, remaining below 3 indicates a good fit[80].

Thioflavin-S (Th-S) aggregation assay

The aggregation of αSyn in the absence or presence of RNA aptamers was evaluated using a Th-S (Sigma–Aldrich) fluorescence assay, as described previously[41]. αSyn and aptamer were dissolved together in RNase-free water (Nacalai; Kyoto, Japan) at 500 µM each and then added to Tris-buffered saline (TBS: 10 mM Tris-HCl, 100 mM KCl, 100 mM NaCl, pH 7.5) to a final concentration of 100 µM for αSyn and 5–50 µM for the aptamer. The mixture was incubated with shaking at 700 rpm at 37 °C in the presence of polytetrafluoroethylene (PTFE) beads (Φ 2.38 mm). For fluorescence measurement, 2.5 µL of the reaction solution was combined with 250 µL of 5 µM Th-S in 5 mM Gly-NaOH (pH 8.5). 1-mM Th-S solution in distilled water was used as a stock solution. These reaction mixtures were frozen and stored at −80 °C in 96-well black plates (ThermoFisher) at designated time points. Fluorescence was measured using a microplate reader (Varioskan LUX multimode microplate reader; ThermoFisher) at λ_{ex} = 430 nm and λ_{em} = 485 nm. All values were normalized by subtracting the background fluorescence of the buffer of aptamer solution without αSyn. The resulting fluorescence values after a 96-h incubation were plotted against concentration using Prism 9.3.1 (GraphPad; San Diego, CA, USA). IC_{50} values were determined via a nonlinear regression analysis. Disaggregation assays were performed by treating preformed fibrils (PFFs), and PTFE beads for 96 hours in the presence of 0.5-fold molar excess 1R6 under the same measurement conditions.

Circular Dichroism (CD) Spectroscopy

CD spectra were measured using a JASCO J-805 Spectroscopy (JASCO, Tokyo, Japan) with a slight modification of a previously described protocol[41]. For RNA measurement, a refolded RNA solution (5 µM, 200 µL) in 10 mM Tris-HCl, pH 7.5, containing 100 mM KCl or LiCl was loaded into a 1-mm pathlength quartz cell (JASCO). For αSyn measurement, 10 µL of a 20 µM αSyn solution, incubated in the same manner as for the Th-S experiments, was loaded into a microsampling disc (JASCO). The CD spectra were recorded at a scanning speed of 100 nm/min between 200 and 320 nm for RNA and 190–260 nm for αSyn, and buffer spectra were subtracted. The CD-NuSS web server (https://project.iith.ac.in/cdnuss/index.html) was used to predict the nucleic acid secondary structures from the CD spectral data using machine learning algorithms developed for the analysis of protein secondary structural composition[57].

Transmission Electron Microscopy (TEM)

The contents of each reaction mixture were examined using TEM after the Th-S assay[41]. For the TEM analysis, each solution was centrifuged at 17,900 *g* for 10 min at 4 °C, and the supernatant was removed. The resulting pellet was resuspended gently in 100 µL ultrapure water using a vortex for 1 min. Fifteen µL of the suspension were applied to a 200-mesh carbon–coated copper grid (Nisshin EM; Tokyo, Japan), incubated for 5 min, and stained twice with 2% uranyl acetate for 1 min. The stained samples were analyzed using a JEM-1400 electron microscope (JEOL, Tokyo, Japan) operating at 100 kV.

Immuno-TEM was performed after incubation of the fibrils of α-syn or its fragments in the presence of biotinylated 1R6. Grids were prepared as described above and incubated with 15 µL of 5 µg/mL anti-biotin antibody (GTX124262, lot No. 40597, GeneTex) for 20 min. The grids were then washed and incubated with 15 µL of 1 µg/mL secondary antibody labeled with 20-nm nanogold particles (BBI Solutions) for 10 min before being negatively stained with 2% uranyl acetate as described above. The stained samples were subjected to TEM at 100 kV.

Dynamic Light Scattering (DLS)

To evaluate the impact of 1R6 on αSyn oligomer/aggregate size, DLS was performed using a Zetasizer Ultra blue (Malvern Instruments, Malvern, UK) at 633 nm incident wavelength and a 174.7° detection angle in the absence or presence of 1R6. Ultrapure water was used as the dispersant at 298 K, yielding a viscosity of 1.33 cP. For protein, the refractive index was 1.45, and the absorption was 0.001. The solutions of αSyn in the absence or presence of the aptamer were prepared in TBS at a final concentration of 60 µM αSyn and/or 20 µM aptamer and then incubated at 37 °C with shaking at 700 rpm in the presence of PTFE beads (Φ 2.38 mm). Each reaction mixture was centrifuged at 20,000 *g* for 10 min at 20 °C, and then the supernatant was removed and measured in triplicate using a disposable plastic microcuvette. The resulting scattering values were analyzed using the ZS Xplorer software v3.20 (Malvern Instruments) to determine the particle size distribution and Z-average.

Photo-induced crosslinking of unmodified proteins (PICUP) assay

PICUP uses visible light to generate Ru^{3+}, an oxidizer that can abstract an electron from a susceptible protein side chain, forming a radical (e.g., Tyr radical) that may covalently bind to another side chain intermolecularly to form a cross-link. PICUP reactions were performed using a slight modification of a previously published protocol[81]. Briefly, 30 µM αSyn was incubated with 6, 15, or 30 µM aptamer in PBS for 30 min at room temperature in a final volume of 7 µL in PCR tubes. Then, 1 µL of 1 mM tris(bipyridyl)ruthenium(II) chloride [$Ru(bpy)_3Cl_2$] and 1 µL of 20 mM ammonium persulfate were added, followed by 1-s irradiation and immediate quenching with 2.5 µL of lithium dodecyl sulfate sample buffer (Invitrogen) containing 50 mM dithiothreitol. Samples were fractionated by electrophoresis on 10% Bis-Tris sodium dodecyl sulfate–polyacrylamide gels (SDS-PAGE; Invitrogen). Non-crosslinked proteins served as controls running as monomers. Protein bands were visualized by silver staining (Wako, Osaka, Japan), scanned

using LuminoGraph II (ATTO, Tokyo, Japan), and quantified densitometrically relative to crosslinked αSyn alone using CS Analyzer4 (ATTO).

Förster resonance energy transfer (FRET)-based biosensor cell seeding assay

αSyn seeding activity was assessed using FRET flow cytometry with a slight modification of a previously published protocol[48]. HEK293T biosensor cell lines, stably expressing full-length αSyn containing the disease-associated A53T substitution fused to either cyan fluorescent protein (CFP) or yellow fluorescent protein (YFP), were a generous gift from Dr. Marc Diamond (University of Texas Southwestern Medical Center, Dallas, TX, USA). CFP-only and YFP-only cells were used as controls. Cells were cultured in Dulbecco's modified Eagle medium (DMEM; Gibco) supplemented with 10% fetal bovine serum (FBS; Nucleus Biologics), 1% PenStrep (Gibco), and 1% GlutaMAX (Gibco) in a humidified incubator at 37 °C with 5% CO_2. For the seeding activity assay, 30,000 cells/well were seeded in 96-well plates. At ~60% confluency (24 h later), seeds containing 20 µg of total protein from MSA mouse brain extracts[47] were prepared by dilution of soluble-fraction brain-lysate samples in OptiMEM (Gibco), sonication for 5 min, and mixing with 8.75 µL OptiMEM +1.25 µL Lipofectamine 2000 (Invitrogen) to a final volume of 20 µL/well. Seed complexes containing 20 µg total protein/well were incubated at room temperature for 30 min before addition to cells. Control cells were incubated with the same solution in the absence of brain extracts. After 72 h, cells were harvested using TrypLE (ThermoFisher), transferred to 96-well round-bottom plates, fixed in 4% paraformaldehyde (Electron Microscopy Services) in PBS for 10 min, and resuspended in flow cytometry buffer (1% FBS, 1 mM EDTA in Hanks' Balanced Salt solution). Fluorescence images were acquired using a BZ-X710 fluorescence microscope (Keyence, Osaka, Japan) and analyzed using BZ-X700 Analyzer software (Keyence).

FRET flow-cytometry was performed using a BD Biosciences LSR II flow cytometer and FACSDiva software. To measure CFP and FRET, cells were excited at 405-nm and captured using 405/50-nm and 525/50-nm filters, respectively. To measure YFP, cells were excited at 488-nm and captured using a 525/50-nm filter. CFP spill-over into YFP and FRET channels was compensated for using CFP-only cells. Flow cytometry data were analyzed using FlowJo v10. To establish the sequential gating hierarchy, intact cells were first gated to exclude cellular debris using a forward scatter area (FSC-A) versus side scatter area (SSC-A) plot[48]. Singlet cells were then strictly isolated from the cell population using an FSC-A versus forward scatter height (FSC-H) plot to exclude doublets and cell aggregates. From this single-cell population, the signal within the FRET filter that arises from the direct activation of YFP by the 405-nm laser was excluded by introducing a "false FRET" gate derived from YFP-only cells. A triangular FRET gate was established with lipofectamine-treated only cells, and the background FRET signal was set at ~1%. Cells that shifted into this gate were FRET+. The integrated FRET density was defined as the percentage of FRET+ cells multiplied by the median fluorescence intensity and standardized by dividing the value of Lipofectamine-only control cells. For each experiment, 20,000 single cells per replicate were analyzed, and each sample was examined in triplicate.

Western blotting

αSyn solutions were mixed with 4× LDS sample buffer (Invitrogen; Carlsbad, CA, USA) before heating at 70 °C for 10 min. The denatured samples were fractionated on NuPAGE 10% Bis-Tris gels (ThermoFisher) and the proteins transferred to PVDF membranes (0.45-µm pore size, Merck Millipore, MA, USA). The membranes were blocked using Blocking Reagent for Can Get Signal (TOYOBO) and incubated with the anti-αSyn primary antibody (ab51252, lot No. GR237394-20, Abcam, 10 µg/mL). The membranes were washed using TB-T, incubated with anti-rabbit secondary antibody, and washed again. Subsequently, blots were developed using enhanced chemiluminescence (ECL Prime, Cytiva; Marlborough, MA, USA) and imaged with Lumino Graph II (ATTO; Tokyo, Japan).

MTT assay

HEK293T cells (RCB2202, RIKEN BioResource Center, Tsukuba, Japan) maintained in DMEM (Wako) containing 10% FBS (Sigma–Aldrich) were used to estimate the neurotoxicity of liposome-encapsulated αSyn exogenously added to the culture medium, as described previously with a slight modification[82]. αSyn, 1R6, or R0 were dissolved in RNase-free water to create a 20x stock solution and diluted in culture medium to the desired concentration. Monomeric αSyn solution containing PFF seeds (5 µg) was combined with 1R6 or R0 and incubated with a transfection reagent (ScreenFect A plus; FUJIFILM Wako, Osaka, Japan) for 20 min at room temperature. The resulting solution (30 µL) was added to the culture medium containing near-confluent cells (1×10^4 cells/well) for overnight adaptation. After 60 hours of incubation at 37 °C, 15 µL/well of Dye solution from the CellTiter 96 Non-Radioactive Cell Proliferation Assay kit (Promega, Madison, WI, USA) was added to the cells and incubated for 3 hours at 37 °C. The reaction was stopped by adding 100 µL/well of solubilization/stop solution, and the cell lysate was incubated in the dark at room temperature overnight. The absorbance was measured at 570 nm using a microplate reader (Varioskan LUX multimode microplate reader; ThermoFisher). The results were normalized to vehicle control (RNase-free water) set as 100% viability.

Drosophila experiments

Construction of transgenic Drosophila and administration of aptamer. Flies were maintained in plastic vials (3-cm diameter, 20-cm height) with standard cornmeal-yeast agar medium at 25 °C in a 12 h light/dark cycle. The *nSyb-Gal4*, *pGMR-Gal4*, *tub-gal80^{ts}*, *pUAS-mCD8-green fluorescent protein (GFP)*, and *P{ninaE.GFP}1* expressing GFP-tagged rhodopsin1 in R1-6 photoreceptor cells under the control of *ninaE* regulatory sequences was obtained from the Bloomington Drosophila Stock Center (Indiana University). Transgenic αSyn flies were generated by cloning human αSyn cDNA into the *pUAST* vector[83] to create a *pUAS-αSyn^{WT}*. A mutant αSyn (αSyn^{S129D}), with serine replaced by aspartic acid at position 129, was inserted into a *pUAST* vector to produce *pUAS-αSyn^{S129D}*. BestGene Inc. injected these vectors to generate the initial strains of *w^{1118}; UAS-αSyn^{WT}* and *w^{1118}; UAS-αSyn^{S129D}*. A *UAS-tau^{R406W}* strain was a generous gift from Dr. Feany[84], and a *UAS-Aβ3–42^{E3Q}* strain was described previously[55].

To induce neuronal expression of αSyn, Aβ3-42^{E3Q} or tau^{R406W} at the adult stage for climbing and life span assays, the *GAL4/UAS/gal-80^{ts}* system was established for the following strains: *nSyb-Gal4/Y; UAS-αSyn^{S129D}/tub-gal80^{ts}; UAS-αSyn^{WT}/+: nSyb-Gal4/Y; UAS-Aβ3-42^{E3Q}/tub-gal80^{ts}: nSyb-Gal4/Y; UAS-tau^{R406W}/tub-gal80^{ts}*. These male flies at the age of 4–7 days were shifted from 18 °C to 29 °C before the experiment[52]. For the neurodegeneration assay (see below), expression of αSyn, Aβ3-42^{E3Q} or tau^{R406W} in compound eyes at the adult stage was induced using the following strains: *pGMR-Gal4, P{ninaE.GFP}1/Y; UAS-αSyn^{S129D}/tub-gal80^{ts}; UASαSyn^{WT}/tub-gal80^{ts}: pGMR-Gal4, P{ninaE.GFP}1/Y; +/tub-gal80^{ts}; UAS-Aβ3-42^{E3Q}/tub-gal80^{ts}: pGMR-Gal4, P{ninaE.GFP}1/Y; UAS-tau^{R406W}/tub-gal80^{ts}; +/tub-gal80^{ts}*. Control strains included: *nSyb-Gal4/Y; UAS-mCD8-GFP/tub-gal80ts; +/+: pGMR-Gal4, P{ninaE.GFP}1/Y; +/tub-gal80^{ts}; +/tub-gal80^{ts}*. The 1R6 aptamer was diluted in 5% sucrose to 5 µM, 25 µM, or 50 µM, and R0 was used at 50 µM. Adult flies were given *ad libitum* access to filter paper soaked with each reagent twice weekly, 2–3 days apart, for 15 hours each time[85].

Climbing assay (Locomotor analysis). In the climbing assay (negative geotaxis assay[86]), 20 flies were placed in an empty plastic vial. The vial

was gently tapped to collect all flies at the bottom, and the number of flies that climbed 5 cm or more within 10 s was recorded. The test was conducted twice with a 15-s interval, and the average value was used as the measurement result.

Lifespan assay. For survival assays, 20 flies per vial were maintained on standard medium at 29 °C, transferred to fresh vials every 2–3 days, and scored for survival. Each experiment was conducted using at least 80–100 flies of each genotype. The results were analyzed using the Kaplan–Meier method and the log-rank test.

Neurodegeneration assay. A 1% agar medium was melted at 100 °C, and anesthetized flies were placed in it when the temperature dropped to 65 °C. After the agar solidified, water was added to immerse the flies. Photoreceptor cell survival was examined under fluorescent light using a 60x water-depth lens and images were captured using a charged-coupled device camera (Olympus, DP-86)[87]. The survival rate was calculated as the ratio of GFP-positive cells (photoreceptor cells) to the number of ommatidia using the following formula:

Survival rate (%) = (number of GFP-positive cells/number of ommatidia x 6) x 100.

ELISA

Fly heads were homogenized in Triton lysis buffer (50 mM Tris-HCl, pH 7.4, 1% Triton X-100, 150 mM NaCl, and 1 mM EDTA) containing protease and phosphatase inhibitor cocktails (Nacalai; Kyoto, Japan) and centrifuged at 15,000 *g* for 20 min at 4 °C to yield Triton-soluble supernatants and Triton-insoluble pellets, as described previously[88]. The pellets were then lysed by sonication in SDS lysis buffer (50 mM Tris-HCl, pH 7.4, 2% SDS, 150 mM NaCl). αSyn levels in the soluble and insoluble fractions were determined using a human αSyn ELISA Kit (catalog # KE00191: ProteinTech, Rosemont, IL, USA) according to the manufacturer's instructions. The absorbance was measured at 450 nm using a microplate reader (Varioskan LUX multimode microplate reader; ThermoFisher).

NMR measurement

^{1}H-^{15}N heteronuclear multiple quantum correlation (HMQC) measurements were performed at 288 K using a Bruker Avance III 800 MHz spectrometer with TCI CryoProbe (Bruker Biospin, Germany). Uniformly ^{15}N-labeled αSyn prepared according to a standard protocol was dissolved at 40 μM in PBS containing 5% D_2O. Refolded aptamer [sh1R6, a short, 21-base fragment of 1R6, synthesized by FASMAC (Kanagawa, Japan)] was added to the αSyn solution at 1–13 equivalents. Peaks were assigned using data in the Biological Magnetic Resonance Data Bank (https://bmrb.io/). The distances between the ^{1}H-^{15}N cross-peaks of αSyn alone or in the presence of different 1R6 concentrations were calculated using the Pythagorean theorem. To account for the different chemical shift ranges of the nuclei, the ^{15}N chemical shifts were scaled by a factor of 0.14 relative to the ^{1}H chemical shifts. Specifically, scaling was applied to the ^{15}N shifts, reflecting their larger chemical shift range compared to ^{1}H. The combined chemical shift perturbation $\Delta\delta_{comb}$ was calculated for quantitative titration using the following equation (https://ccpn.ac.uk/manual/v3/Titrations.html):

$$\Delta_{\delta comb} = \sqrt{\frac{(\Delta_{\delta H})^2 + (0.14 \times \Delta_{\delta N})^2}{2}}$$

The NMR titration data were fitted and simulated using the TITAN software package (https://nmr-titan.com/citing.html).

In silico molecular docking

The secondary structure of the aptamer was predicted using Mfold and modeled with FARFAR2 in Rosetta[89]. The template structures were selected from the ONQUADRO database[90] based on the sequence similarities of the subsequences, which were calculated using an in-house Python script. The structures with the highest scores were docked on αSyn. In its monomeric form, αSyn may adopt an α-helical structure, especially when bound to membranes, whereas in its aggregated form, it forms β-sheet-rich fibrils. Protein Data Bank (PDB) entries with long solved regions were selected as follows: αSyn monomer (PDB code: 1XQ8); αSyn fibril structures (PDB codes: 2N0A or 6XYO); Aβ42 fibril structures (PDB code: 2NAO and 2MXU). Structural models were generated using AlphaFold3 (AF3) (Supplementary Fig. S17). The full-length tau protein sequence (441 residues; UniProt: P10636-8, isoform 2N4R) was used without truncation or modification. The highest-ranking model, as determined by the ranking score, was selected for analysis. Model confidence was evaluated using per-residue pLDDT values and predicted aligned error (PAE). Given the intrinsically disordered nature of tau, the model is interpreted qualitatively.

For fibril structures, the first chain was used for docking. The docking calculations were performed using HADDOCK2.4[91]. Twenty structures were generated for each docking process, and the best-scoring models were selected using HADDOCK scores, as the structures did not form a single dominant cluster, indicating multiple plausible docking models.

Statistical analysis

Statistical analysis was performed using Welch's *t*-test or one-way analysis of variance (ANOVA) followed by Dunnett's or Tukey's post-hoc test, as appropriate in Prism version 9.3.1 (GraphPad).

Reporting summary

Further information on research design is available in the Nature Portfolio Reporting Summary linked to this article.

Data availability

Unless otherwise stated, all data supporting the results of this study can be found in the article, supplementary, and source data files. The PDB accession codes used in this study are listed below: 1XQ8, 2N0A, 6XYO, 6L1U, 5OQV, 6QJH, 2NAO, 2MXU. The RNA-seq dataset generated in this study has been deposited in the NCBI Sequence Read Archive (SRA) under BioProject accession number PRJNA1479858. This dataset contains raw FASTQ files generated from SELEX experiments for α-synuclein-binding RNA aptamers. Following enrichment of bound RNA pools and RT-PCR amplification, amplicon DNA libraries were prepared using the TruSeq Nano DNA Kit (Illumina, San Diego, CA, USA). Next-generation sequencing was performed on the NovaSeq 6000 platform (Illumina, San Diego, CA, USA) at Macrogen Japan Corp. (Tokyo, Japan). The dataset includes raw sequencing reads from rounds 0 and 6 of SELEX in compressed FASTQ format, together with accompanying metadata. Source data are provided with this paper.

References

1. Emamzadeh, F. N. Alpha-synuclein structure, functions, and interactions. *J. Res. Med. Sci.* **21**, 29 (2016).
2. Calabresi, P., Mechelli, A., Natale, G., Volpicelli-Daley, L., Di Lazzaro, G. & Ghiglieri, V. Alpha-synuclein in Parkinson's disease and other synucleinopathies: from overt neurodegeneration back to early synaptic dysfunction. *Cell Death Dis.* **14**, 176 (2023).
3. Kuo, G., Kumbhar, R., Blair, W., Dawson, V. L., Dawson, T. M. & Mao, X. Emerging targets of alpha-synuclein spreading in alpha-synucleinopathies: a review of mechanistic pathways and interventions. *Mol. Neurodegener.* **20**, 10 (2025).
4. Breydo, L., Wu, J. W. & Uversky, V. N. Alpha-synuclein misfolding and Parkinson's disease. *Biochim. Biophys. Acta* **1822**, 261–285 (2012).
5. Nussbaum, R. L. Polymeropoulos MH. Genetics of Parkinson's disease. *Hum. Mol. Genet.* **6**, 1687–1691 (1997).

6. Spillantini, M. G., Schmidt, M. L., Lee, V. M., Trojanowski, J. Q., Jakes, R. & Goedert, M. Alpha-synuclein in Lewy bodies. *Nature* **388**, 839–840 (1997).
7. Trojanowski, J. Q., Goedert, M., Iwatsubo, T. & Lee, V. M. Fatal attractions: abnormal protein aggregation and neuron death in Parkinson's disease and Lewy body dementia. *Cell Death Differ.* **5**, 832–837 (1998).
8. Kruger, R. et al. Ala30Pro mutation in the gene encoding alpha-synuclein in Parkinson's disease. *Nat. Genet.* **18**, 106–108 (1998).
9. Du, X. Y., Xie, X. X. & Liu, R. T. The role of α-synuclein oligomers in Parkinson's disease. *Int. J. Mol. Sci.* **21**, 8645 (2020).
10. Goedert, M. Alpha-synuclein and neurodegenerative diseases. *Nat. Rev. Neurosci.* **2**, 492–501 (2001).
11. Goedert M. NEURODEGENERATION. Alzheimer's and Parkinson's diseases: The prion concept in relation to assembled Abeta, tau, and alpha-synuclein. *Science* **349**, 1255555 (2015).
12. Uemura, N., Uemura, M. T., Luk, K. C., Lee, V. M. & Trojanowski, J. Q. Cell-to-Cell Transmission of Tau and alpha-Synuclein. *Trends Mol. Med.* **26**, 936–952 (2020).
13. Winner, B. et al. In vivo demonstration that alpha-synuclein oligomers are toxic. *Proc. Natl. Acad. Sci. USA.* **108**, 4194–4199 (2011).
14. Doherty, C. P. A. et al. A short motif in the N-terminal region of alpha-synuclein is critical for both aggregation and function. *Nat. Struct. Mol. Biol.* **27**, 249–259 (2020).
15. Zarbiv, Y., Simhi-Haham, D., Israeli, E., Elhadi, S. A., Grigoletto, J. & Sharon, R. Lysine residues at the first and second KTKEGV repeats mediate alpha-Synuclein binding to membrane phospholipids. *Neurobiol. Dis.* **70**, 90–98 (2014).
16. Dettmer, U., Newman, A. J., von Saucken, V. E., Bartels, T. & Selkoe, D. KTKEGV repeat motifs are key mediators of normal alpha-synuclein tetramerization: their mutation causes excess monomers and neurotoxicity. *Proc. Natl. Acad. Sci. USA.* **112**, 9596–9601 (2015).
17. Farzadfard, A. et al. The C-terminal tail of alpha-synuclein protects against aggregate replication but is critical for oligomerization. *Commun. Biol.* **5**, 123 (2022).
18. Schweighauser, M. et al. Structures of alpha-synuclein filaments from multiple system atrophy. *Nature* **585**, 464–469 (2020).
19. McGlinchey, R. P., Shewmaker, F., Hu, K. N., McPhie, P., Tycko, R. & Wickner, R. B. Repeat domains of melanosome matrix protein Pmel17 orthologs form amyloid fibrils at the acidic melanosomal pH. *J. Biol. Chem.* **286**, 8385–8393 (2011).
20. Tripathi, T. A master regulator of α-synuclein aggregation. *ACS Chem. Neurosci.* **11**, 1376–1378 (2020).
21. Mahul-Mellier, A. L. et al. Differential role of C-terminal truncations on alpha-synuclein pathology and Lewy body formation. *NPJ Parkinsons Dis.* **11**, 261 (2025).
22. Baba, M. et al. Aggregation of alpha-synuclein in Lewy bodies of sporadic Parkinson's disease and dementia with Lewy bodies. *Am. J. Pathol.* **152**, 879–884 (1998).
23. Sorrentino, Z. A. & Giasson, B. I. The emerging role of alpha-synuclein truncation in aggregation and disease. *J. Biol. Chem.* **295**, 10224–10244 (2020).
24. Wiseman, J. A., Halliday, G. M. & Dieriks, B. V. Neuronal alpha-synuclein toxicity is the key driver of neurodegeneration in multiple system atrophy. *Brain* **148**, 2306–2319 (2025).
25. Zhou, J. & Rossi, J. Aptamers as targeted therapeutics: current potential and challenges. *Nat. Rev. Drug Discov.* **16**, 181–202 (2017).
26. Murakami, K., Izuo, N. & Bitan, G. Aptamers targeting amyloidogenic proteins and their emerging role in neurodegenerative diseases. *J. Biol. Chem.* **298**, 101478 (2022).
27. Ginsberg, S. D., Galvin, J. E., Chiu, T. S., Lee, V. M., Masliah, E. & Trojanowski, J. Q. RNA sequestration to pathological lesions of neurodegenerative diseases. *Acta Neuropathol.* **96**, 487–494 (1998).
28. Ginsberg, S. D. et al. Predominance of neuronal mRNAs in individual Alzheimer's disease senile plaques. *Ann. Neurol.* **45**, 174–181 (1999).
29. Hua, Q. et al. Microtubule associated protein tau binds to double-stranded but not single-stranded DNA. *Cell. Mol. Life Sci.* **60**, 413–421 (2003).
30. Rahimi, F., Murakami, K., Summers, J. L., Chen, C. H. & Bitan, G. RNA aptamers generated against oligomeric Abeta40 recognize common amyloid aptatopes with low specificity but high sensitivity. *PLoS One* **4**, e7694 (2009).
31. Tsukakoshi, K., Harada, R., Sode, K. & Ikebukuro, K. Screening of DNA aptamer that binds to alpha-synuclein. *Biotechnol. Lett.* **32**, 643–648 (2010).
32. Tsukakoshi, K. et al. Structural regulation by a G-quadruplex ligand increases binding abilities of G-quadruplex-forming aptamers. *Chem. Commun.* **52**, 12646–12649 (2016).
33. Zheng, Y. et al. Novel DNA aptamers for Parkinson's disease treatment inhibit α-synuclein aggregation and facilitate its degradation. *Mol. Ther. Nucleic Acids* **11**, 228–242 (2018).
34. Tartaglia, G. G. & Vendruscolo, M. The Zyggregator method for predicting protein aggregation propensities. *Chem. Soc. Rev.* **37**, 1395–1401 (2008).
35. Thompson, M. J., Sievers, S. A., Karanicolas, J., Ivanova, M. I., Baker, D. & Eisenberg, D. The 3D profile method for identifying fibril-forming segments of proteins. *Proc. Natl. Acad. Sci. USA.* **103**, 4074–4078 (2006).
36. Sormanni, P., Aprile, F. A. & Vendruscolo, M. The CamSol method of rational design of protein mutants with enhanced solubility. *J. Mol. Biol.* **427**, 478–490 (2015).
37. Heid, LF, Kupreichyk, T, Schutzmann, MP, Schneider, W, Stoldt, M, Hoyer, W. Nucleation of alpha-Synuclein amyloid fibrils induced by cross-interaction with beta-hairpin peptides derived from immunoglobulin light chains. *Int. J. Mol. Sci.* **24**, 16132 (2023).
38. Serio, T. R. et al. Nucleated conformational conversion and the replication of conformational information by a prion determinant. *Science* **289**, 1317–1321 (2000).
39. Murakami, K. & Ono, K. Interactions of amyloid coaggregates with biomolecules and its relevance to neurodegeneration. *FASEB J.* **36**, e22493 (2022).
40. Sugimoto, S., Arita-Morioka, K., Mizunoe, Y., Yamanaka, K. & Ogura, T. Thioflavin T as a fluorescence probe for monitoring RNA metabolism at molecular and cellular levels. *Nucleic Acids Res.* **43**, e92 (2015).
41. Murakami, K. et al. An RNA aptamer with potent affinity for a toxic dimer of amyloid β42 has potential utility for histochemical studies of Alzheimer's disease. *J. Biol. Chem.* **295**, 4870–4880 (2020).
42. Bitan, G., Kirkitadze, M. D., Lomakin, A., Vollers, S. S., Benedek, G. B. & Teplow, D. B. Amyloid beta -protein (Abeta) assembly: Abeta 40 and Abeta 42 oligomerize through distinct pathways. *Proc. Natl. Acad. Sci. USA.* **100**, 330–335 (2003).
43. Bitan, G. Structural study of metastable amyloidogenic protein oligomers by photo-induced cross-linking of unmodified proteins. *Methods Enzymol.* **413**, 217–236 (2006).
44. Acharya, S. et al. Molecular basis for preventing alpha-synuclein aggregation by a molecular tweezer. *J. Biol. Chem.* **289**, 10727–10737 (2014).
45. Ortigosa-Pascual, L., Leiding, T., Linse, S. & Palmadottir, T. Photo-induced cross-linking of unmodified alpha-Synuclein Oligomers. *ACS Chem. Neurosci.* **14**, 3192–3205 (2023).
46. Oueslati, A., Ximerakis, M. & Vekrellis, K. Protein transmission, seeding and degradation: key steps for alpha-Synuclein Prion-like propagation. *Exp. Neurobiol.* **23**, 324–336 (2014).
47. Herrera-Vaquero, M. et al. The molecular tweezer CLR01 reduces aggregated, pathologic, and seeding-competent alpha-synuclein

in experimental multiple system atrophy. *Biochim Biophys. Acta Mol. Basis Dis.* **1865**, 165513 (2019).
48. Maina, K. N., Smet-Nocca, C. & Bitan, G. Using FRET-based biosensor cells to study the seeding activity of Tau and alpha-Synuclein. *Methods Mol. Biol.* **2551**, 125–145 (2023).
49. Desplats, P. et al. Inclusion formation and neuronal cell death through neuron-to-neuron transmission of alpha-synuclein. *Proc. Natl. Acad. Sci. USA.* **106**, 13010–13015 (2009).
50. Luk, K. C. et al. Exogenous alpha-synuclein fibrils seed the formation of Lewy body-like intracellular inclusions in cultured cells. *Proc. Natl. Acad. Sci. USA.* **106**, 20051–20056 (2009).
51. Febbraro, F. et al. Ser129D mutant alpha-synuclein induces earlier motor dysfunction while S129A results in distinctive pathology in a rat model of Parkinson's disease. *Neurobiol. Dis.* **56**, 47–58 (2013).
52. Zeidler, M. P. et al. Temperature-sensitive control of protein activity by conditionally splicing inteins. *Nat. Biotechnol.* **22**, 871–876 (2004).
53. Sofola, O. et al. Inhibition of GSK-3 ameliorates Abeta pathology in an adult-onset Drosophila model of Alzheimer's disease. *PLoS Genet.* **6**, e1001087 (2010).
54. Crowther, D. C. et al. Intraneuronal Abeta, non-amyloid aggregates and neurodegeneration in a Drosophila model of Alzheimer's disease. *Neuroscience* **132**, 123–135 (2005).
55. Tsuda, L., Omata, Y., Yamasaki, Y., Minami, R. & Lim, Y. M. Pyroglutamate-amyloid-beta peptide expression in Drosophila leads to caspase-dependent and endoplasmic reticulum stress-related progressive neurodegeneration. *Hum. Mol. Genet.* **26**, 4642–4656 (2017).
56. Hutton, M. et al. Association of missense and 5'-splice-site mutations in tau with the inherited dementia FTDP-17. *Nature* **393**, 702–705 (1998).
57. Sathyaseelan, C., Vijayakumar, V. & Rathinavelan, T. CD-NuSS: a web server for the automated secondary structural characterization of the nucleic acids from circular dichroism spectra using extreme gradient boosting decision-tree, neural network and Kohonen algorithms. *J. Mol. Biol.* **433**, 166629 (2021).
58. de Vries, S. J., van Dijk, M. & Bonvin, A. M. The HADDOCK web server for data-driven biomolecular docking. *Nat. Protoc.* **5**, 883–897 (2010).
59. Bartels, T. et al. The N-terminus of the intrinsically disordered protein alpha-synuclein triggers membrane binding and helix folding. *Biophys. J.* **99**, 2116–2124 (2010).
60. Crowther, R. A., Jakes, R., Spillantini, M. G. & Goedert, M. Synthetic filaments assembled from C-terminally truncated alpha-synuclein. *FEBS Lett.* **436**, 309–312 (1998).
61. Izawa, Y. et al. Role of C-terminal negative charges and tyrosine residues in fibril formation of alpha-synuclein. *Brain Behav.* **2**, 595–605 (2012).
62. Masuda, M. et al. Inhibition of alpha-synuclein fibril assembly by small molecules: analysis using epitope-specific antibodies. *FEBS Lett.* **583**, 787–791 (2009).
63. Alfaidi, M., Barker, R. A. & Kuan, W. L. An update on immune-based alpha-synuclein trials in Parkinson's disease. *J. Neurol.* **272**, 21 (2024).
64. Lang, A. E. et al. Trial of Cinpanemab in early Parkinson's disease. *N. Engl. J. Med.* **387**, 408–420 (2022).
65. Santos, J. et al. alpha-Helical peptidic scaffolds to target alpha-synuclein toxic species with nanomolar affinity. *Nat. Commun.* **12**, 3752 (2021).
66. Kritzer, J. A. et al. Rapid selection of cyclic peptides that reduce alpha-synuclein toxicity in yeast and animal models. *Nat. Chem. Biol.* **5**, 655–663 (2009).
67. Ikenoue, T. et al. De Novo peptides that induce the liquid-liquid phase separation of alpha-Synuclein. *J. Am. Chem. Soc.* **147**, 24113–24126 (2025).
68. Zhou, M., Li, Q. & Wang, R. Current experimental methods for characterizing protein-protein interactions. *ChemMedChem* **11**, 738–756 (2016).
69. Rich, R. L. & Myszka, D. G. Survey of the year 2000 commercial optical biosensor literature. *J. Mol. Recognit.* **14**, 273–294 (2001).
70. Li, H, Rahimi, F, Murakami, K, Maiti, P, Sinha, S, Bitan, G. Amyloids and protein aggregation –analytical methods. *Encyclopedia of Analytical Chemistry*, RA Meyers (*Ed.) John Wiley & Sons Ltd.*, 635–666 (2009).
71. Hmila, I. et al. Inhibition of alpha-Synuclein seeding-dependent aggregation by ssDNA Aptamers specific to C-Terminally truncated alpha-Synuclein fibrils. *ACS Chem. Neurosci.* **13**, 3330–3341 (2022).
72. Ghanem, S. S. et al. alpha-Synuclein phosphorylation at serine 129 occurs after initial protein deposition and inhibits seeded fibril formation and toxicity. *Proc. Natl. Acad. Sci. USA.* **119**, e2109617119 (2022).
73. Crombez, L. et al. A new potent secondary amphipathic cell-penetrating peptide for siRNA delivery into mammalian cells. *Mol. Ther.* **17**, 95–103 (2009).
74. Ren, X. et al. Exosomal DNA aptamer targeting α-synuclein aggregates reduced neuropathological deficits in a mouse Parkinson's disease model. *Mol. Ther. Nucleic Acids* **17**, 726–740 (2019).
75. Zekry, D., Hauw, J. J. & Gold, G. Mixed dementia: epidemiology, diagnosis, and treatment. *J. Am. Geriatr. Soc.* **50**, 1431–1438 (2002).
76. Irwin, D. J., Lee, V. M. & Trojanowski, J. Q. Parkinson's disease dementia: convergence of alpha-synuclein, tau and amyloid-beta pathologies. *Nat. Rev. Neurosci.* **14**, 626–636 (2013).
77. Moussaud, S., Jones, D. R., Moussaud-Lamodiere, E. L., Delenclos, M., Ross, O. A. & McLean, P. J. Alpha-synuclein and tau: teammates in neurodegeneration?. *Mol. Neurodegener.* **9**, 43 (2014).
78. McKeague, M. et al. The minimum aptamer publication standards (MAPS guidelines) for de novo aptamer selection. *Aptamers* **6**, 10–18 (2022).
79. Sawner, A. S. et al. Modulating alpha-Synuclein Liquid-Liquid Phase Separation. *Biochemistry* **60**, 3676–3696 (2021).
80. Apiyo, D. Biomolecular binding kinetics assays on the Octet BLI platform. *Sartorius Appl. Note.* https://www.sartorius.com/resource/blob/742330/05671fe2de45d16bd72b8078ac28980d/octet-biomolecular-binding-kinetics-application-note-4014-en-1--data.pdf (2022).
81. Rosensweig, C., Ono, K., Murakami, K., Lowenstein, D. K., Bitan, G. & Teplow, D. B. Preparation of stable amyloid beta-protein oligomers of defined assembly order. *Methods Mol. Biol.* **849**, 23–31 (2012).
82. Prabhudesai, S. et al. A novel "molecular tweezer" inhibitor of alpha-synuclein neurotoxicity in vitro and in vivo. *NeuroTher.: J. Am. Soc. Exp. NeuroTher.* **9**, 464–476 (2012).
83. Brand, A. H. & Perrimon, N. Targeted gene expression as a means of altering cell fates and generating dominant phenotypes. *Development* **118**, 401–415 (1993).
84. Wittmann, C. W. et al. Tauopathy in Drosophila: neurodegeneration without neurofibrillary tangles. *Science* **293**, 711–714 (2001).
85. Yamasaki, Y., Tsuda, L., Suzuki, A. & Yanagisawa, K. Induction of ganglioside synthesis in Drosophila brain accelerates assembly of amyloid beta protein. *Sci. Rep.* **8**, 8345 (2018).
86. Iijima, K. et al. Abeta42 mutants with different aggregation profiles induce distinct pathologies in Drosophila. *PLoS One* **3**, e1703 (2008).
87. Pichaud, F. & Desplan, C. A new visualization approach for identifying mutations that affect differentiation and organization of the Drosophila ommatidia. *Development* **128**, 815–826 (2001).
88. Suzuki, M. et al. Glucocerebrosidase deficiency accelerates the accumulation of proteinase K-resistant alpha-synuclein and aggravates neurodegeneration in a Drosophila model of Parkinson's disease. *Hum. Mol. Genet.* **24**, 6675–6686 (2015).

89. Watkins, A. M., Rangan, R. & Das, R. FARFAR2: Improved De Novo Rosetta prediction of complex Global RNA folds. *Structure* **28**, 963–976 .e966 (2020).
90. Zok, T., Kraszewska, N., Miskiewicz, J., Pielacinska, P., Zurkowski, M. & Szachniuk, M. ONQUADRO: a database of experimentally determined quadruplex structures. *Nucleic Acids Res.* **50**, D253–D258 (2022).
91. Honorato, R. V. et al. The HADDOCK2.4 web server for integrative modeling of biomolecular complexes. *Nat. Protoc.* **19**, 3219–3241 (2024).

Acknowledgements

We thank Ms. M. Kato (Malvern Panalytical Ltd., Malvern, UK) for technical assistance with DLS measurements. The authors would like to thank Enago (www.enago.jp) for the English language review.

Author contributions

K.Mu. conceptualized the research, designed the research, performed aptamer development, supervised the overall study, and wrote the original manuscript; T.H.V.N. performed aptamer development; L.T. performed fly experiments; E.C. performed FRET experiments; Y.W. contributed reagents/analytic tools; Y.C. performed NMR experiments; N.S. contributed reagents/analytic tools; C.N. performed bioinformatics; K.Mi. supervised bioinformatics; S.M. and S.K.M. contributed reagents/analytic tools; H.T. supervised NMR experiments; G.B. supervised FRET experiments, conceptualized the research, and wrote the original manuscript. The manuscript was written through the contributions of all authors. All authors have read, edited, and given approval to the final version of the manuscript.

Funding

This study was supported in part by the JSPS KAKENHI, grant number 20KK0126, 23K26786, and 23H03852 to K. M. and NIH/NIA RF1AG054000 to G. B.

Competing interests

The authors declare no competing interests.

Additional information

Supplementary information The online version contains supplementary material available at https://doi.org/10.1038/s41467-026-75209-z.

Correspondence and requests for materials should be addressed to Kazuma Murakami.

Peer review information *Nature Communications* thanks Kanae Ando, who co-reviewed with Jun-qi Huangand the other, anonymous, reviewer(s) for their contribution to the peer review of this work. A peer review file is available.